UNIVERSITY OF CALIFORNIA, SAN DIEGO

Plasmonics for Super Resolution Optical Imaging

A dissertation submitted in partial satisfaction of the
requirements for the degree
Doctor of Philosophy

in

Electrical Engineering (Applied Physics)

by

Joseph Louis Ponsetto

Committee in charge:

Professor Zhaowei Liu, Chair
Professor Joseph Ford
Professor Ratneshwar Lal
Professor George Papen
Professor Donald Sirbuly

2016

The dissertation of Joseph Louis Ponsetto is approved, and it is acceptable in quality and form for publication on microfilm and electronically:

_____

_____

_____

_____

_____
Chair

University of California, San Diego

2016

DEDICATION

To my family, for their love and support.

EPIGRAPH

Truth is ever to be found in simplicity,

and not in the multiplicity and confusion of things.

– Isaac Newton

TABLE OF CONTENTS

LIST OF FIGURES

ACKNOWLEDGEMENTS

To my advisor, Professor Zhaowei Liu, I thank you sincerely for your support. From the moment I joined your research group, I have appreciated your tireless energy and optimism. I have learned a lot from you, both from your direct teaching in technical matters, and from more indirect observation of your skills with things like time-management, self-motivation, and leadership. I will always be grateful.

To my Ph.D. Committee, thank you for being a part of my doctoral studies here at UCSD. Your comments and insight at my qualifying exam and throughout the past few years have always been helpful.

To all of my colleagues, thank you for your generous help with various aspects of my project. Thank you for the fruitful technical discussions, and thank you for the equally fruitful idle chat and friendly company, which made long hours in the lab more enjoyable.

Lastly, thank you to all of my family, friends, and loved ones. Having such great people to be with during this period of my life was a constant source of strength.

Chapter 2, in part, is a reprint of the material as it appears in Nanoscale, 2014, 6, 5807-5812. Joseph L. Ponsetto, Feifei Wei, Zhaowei Liu, "Localized plasmon assisted structured illumination microscopy for wide-field high-speed dispersion-independent super resolution imaging". The dissertation author was the first author of this paper.

Chapter 3, in part, is a reprint of the material as submitted to Nature Photonics, 2016. Joseph L. Ponsetto, Anna S. Bezryadina, Feifei Wei, Keisuke Onishi, Hao Shen, Eric Huang, Lorenzo Ferrari, Qian Ma, Yimin Zou, Zhaowei Liu, "Experimental demonstration of wide-field super resolution surface imaging with localized plasmonic structured illumination microscopy". The dissertation author was the first author of this paper.

Chapter 4, in part, is a reprint of the material as it appears in Optics Express, 2015,

23, 18501-18510. Weiwei Wan[†], Joseph L. Ponsetto[†], Zhaowei Liu, "Numerical study of hyperlenses for three-dimensional imaging and lithography" [[†]Equal contribution]. The dissertation author was the co-first author of this paper.

VITA

2010	B. S. in Physics, Boston College, Chestnut Hill
2012	M. S in Electrical Engineering (Applied Physics), University of California, San Diego
2016	Ph. D. in Electrical Engineering (Applied Physics), University of California, San Diego

PUBLICATIONS

Joseph L. Ponsetto, Anna S. Bezryadina, Feifei Wei, Keisuke Onishi, Hao Shen, Eric Huang, Lorenzo Ferrari, Qian Ma, Yimin Zou, Zhaowei Liu, "Experimental demonstration of wide-field super resolution surface imaging with localized plasmonic structured illumination microscopy", *Submitted to Nature Photonics*.

Joseph L. Ponsetto, Dylan Lu, Zhaowei Liu, "The far-field superlens", *Pan Stanford Publishing*, In preparation.

Weiwei Wan[†], Joseph L. Ponsetto[†], Zhaowei Liu, "Numerical study of hyperlenses for three-dimensional imaging and lithography", *Optics Express*, 2015. [[†]Equal contribution]

Joseph L. Ponsetto, Feifei Wei, Zhaowei Liu, "Localized plasmon assisted structured illumination microscopy", *SPIE Optics + Photonics*, 2014.

Feifei Wei, Joseph L. Ponsetto, Zhaowei Liu, "Plasmonic structured illumination microscopy", *Pan Stanford Publishing*, In preparation.

Anna S. Bezryadina, Joseph L. Ponsetto, Zhaowei Liu, "Movable microlenses for localized plasmon structured illumination microscopy", *SPIE Optics + Photonics*, 2016.

Feifei Wei, Dylan Lu, Hao Shen, Weiwei Wan, Joseph L. Ponsetto, Eric Huang, Zhaowei Liu, "Wide field super-resolution surface imaging through plasmonic structured illumination microscopy", *Nano Letters*, 2014.

Joseph L. Ponsetto, Feifei Wei, Zhaowei Liu, "Localized plasmon assisted structured illumination microscopy for wide-field high-speed dispersion-independent super resolution imaging", *Nanoscale*, 2014.

Andreas O. J. Wiberg, Zhi Tong, Lan Liu, Joseph L. Ponsetto, Vahid Ataie, Evgeny Myslivets, Nikola Alic, Stojan Radic, "Demonstration of parallel polychromatic sampling based analog-to-digital conversion at 8 GS/s", *Conference on Lasers and Electro-Optics*, 2012.

Andreas O. J. Wiberg, Zhi Tong, Lan Liu, Joseph L. Ponsetto, Vahid Ataie, Evgeny Myslivets, Nikola Alic, Stojan Radic, "Demonstration of 40 GHz analog-to-digital conversion using copy-and-sample-all parametric processing", *Optical Fiber Communication Conference*, 2012.

Wenchen Chen, Atcha Totachawattana, Kebin Fan, Joseph L. Ponsetto, Andrew C. Strikwerda, Xin Zhang, Richard D. Averitt, Willie J. Padilla, "Single-layer terahertz metamaterials with bulk optical constants", *Physical Review B*, 2012

ABSTRACT OF THE DISSERTATION

Plasmonics for Super Resolution Optical Imaging

by

Joseph Louis Ponsetto

Doctor of Philosophy in Electrical Engineering (Applied Physics)

University of California, San Diego, 2016

Professor Zhaowei Liu, Chair

Imaging with resolution beyond the diffraction limit has attracted great interest in recent years. In this work, new tools for super resolution optical imaging using plasmonics are developed and demonstrated theoretically and/or experimentally: Localized Plasmonic Structured Illumination Microscopy (LPSIM) and the hyperlens.

The LPSIM technique offers a significant improvement in resolution performance over existing structured illumination microscopy (SIM) methods. An array of plasmonic nano-antennas provide dynamically tunable near-field excitations, which result in a finely structured illumination pattern for a given fluorescent object of interest. The illumination

pattern feature sizes are limited only by the antenna geometry, and reconstruction from simple far-field images yields deeply subwavelength resolution. In the initial theoretical and experimental demonstrations shown, resolution is improved 3-fold relative to the diffraction limit. LPSIM is attractive among competing tools due to its wide field of view, bio-compatibility, and video-rate speed capability.

Imaging applications of the hyperlens are also shown in this work. A spherical, metal-dielectric multilayer geometry is used to numerically demonstrate unprecedented radial resolution at 5 nm scale for both imaging and lithography applications. Accuracy far beyond the diffraction limit in the radial direction indicates potential for three-dimensional imaging and lithography applications. Design optimization with regards to several important hyperlens parameters is explored in detail.

Chapter 1

Introduction

Before jumping directly into the technical details of localized plasmonic structured illumination microscopy (LPSIM) and the hyperlens, some of the major supporting principles will be introduced. The concept of the diffraction limit, its significance, and its origin will be explained. The original technique of structured illumination microscopy (SIM) will be summarized, and its achievements and limitations will be discussed. Finally in this chapter, a brief introduction to plasmonics and their physical characteristics will be given.

1.1 The diffraction limit

A standard microscope allows us to capture an image with high resolution. The primary mechanism for achieving this is magnification. For a detector with a given pixel size, an object can be seen with higher resolution if it is magnified such that its image takes up a larger area on the detector. But neither an infinitely-magnified image, nor an infinite pixel density will yield an image with infinite resolution. There is a limit to this type of resolution improvement, and it comes fundamentally from the wave-like behavior of light.

Christiaan Huygens proposed in 1678 [Huy78] that the wavefront motion of propagating light is determined by spherical wavelets originating from every point on the wavefront at the previous instant in time. This idea, known as Huygens' principle, is a very useful tool for predicting the way a wave will respond to any local geometry. For example, consider a wall with a small gap in it (as shown in Fig. 1.1). A plane wave traveling straight at the wall will spread out after passing through the gap, due to Huygens' principle. This is an example of diffraction.

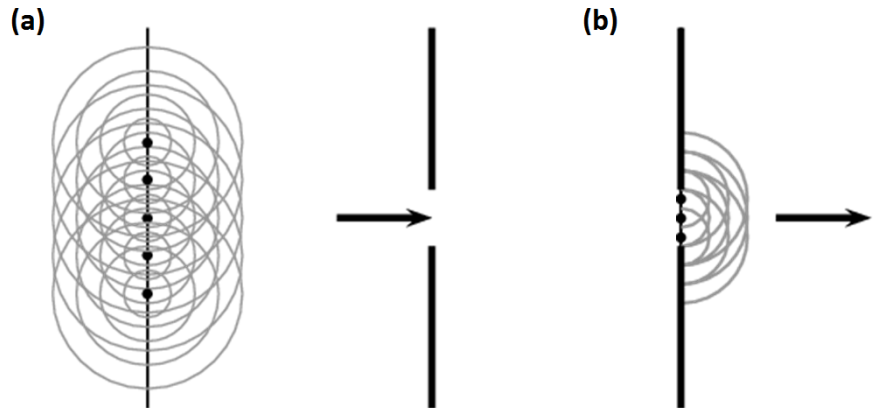

Figure 1.1: Huygens' principle: a wave disturbance passing through a slit will spread out from the shadow of the slit in a process called diffraction. This behavior can be explained by Huygens' principle. [Siy16]

Let us examine this single-slit problem in more detail. For a more realistic situation, we can think instead of a small two-dimensional circular aperture in an opaque surface. Each point on the wavefront passing through the aperture will propagate outwards in all directions as a point source on the other side. Calculating the wavefront analytically at a given point in space can be fairly involved. If we wish to observe the diffraction pattern in the far-field, we can adopt the approximations of Fraunhofer diffraction. It can then be shown [BW99] that the far-field diffraction pattern is simply a scaled inverse Fourier transform of the aperture itself. Thus, for the case of a circular aperture, we are left with a diffraction pattern in the

form of an Airy disc, as shown in Fig. 1.2.

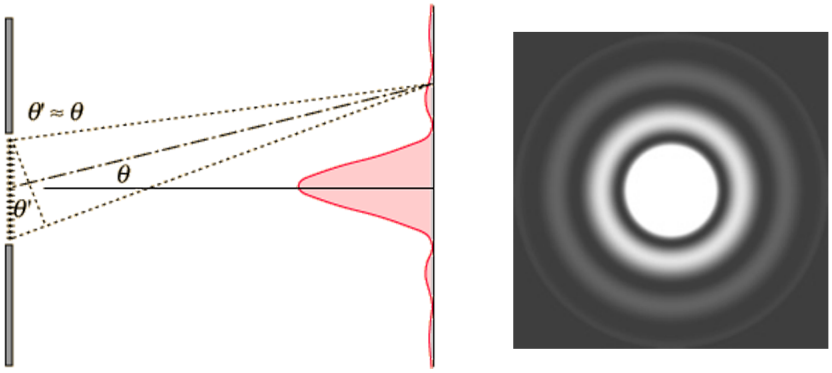

Figure 1.2: Airy disc diffraction: For light diffracting from a circular aperture or source, an Airy disc pattern will be formed in the far-field. The maxima and minima of the diffraction pattern correspond to constructive and destructive interference conditions, respectively. [Mar13]

This pattern can be calculated mathematically by taking the Fourier transform of the circular aperture. It can also be justified intuitively by considering the trigonometry which dictates the alternating constructive and destructive interference of the wavelets traveling from the aperture to the plane of observation, as a function of the angle θ in Fig. 1.2. The angle at which the first minimum of the diffraction pattern occurs is approximately

$$\theta = \sin^{-1}\left(1.22\frac{\lambda}{d}\right) \tag{1.1}$$

Where d is the aperture diameter and λ is the wavelength of the light. For small angles, we can further approximate Eq. 1.1 and write

$$\theta = 1.22\frac{\lambda}{d} \tag{1.2}$$

We can see clearly from this equation that the width of the central peak of the Airy

disc will be inversely related to the aperture size. In most imaging setups, a circular lens is used to focus an image to a detector of some kind. In this case, the aperture we are concerned with is the aperture of the lens.

The reason we are so interested in this Airy disc diffraction pattern is that it will determine the resolution of an imaging system. We have so far talked about a circular aperture as a source of light, but the same analysis applies to any small circular or point-like source. Even larger sources of light can be considered to be a sum of many point sources. With this in mind, the focused image obtained from a point source becomes a critical characteristic of any imaging system, and is called the point spread function (PSF).

There are many ways to describe the resolution performance of a microscope, but one of the most common is the Rayleigh criterion, which defines the resolution limit due to diffraction as the separation at which the principal diffraction maximum of one point source image overlaps the first minimum of another. This condition is described by Eq. 1.2. Thus we can describe the minimum resolvable distance between two points as

$$\delta = \frac{0.61\lambda}{NA} \tag{1.3}$$

where NA is the numerical aperture

$$NA = n\sin(\phi) \tag{1.4}$$

with n as the index of refraction of the surrounding media, and ϕ as half the angular aperture of the lens or microscope objective. This relatively simple equation gives us good intuitive insight into the key factors determining the diffraction limit of a system.

If the illuminating wavelength is decreased, the resolution of a diffraction-limited

system will improve. This is, for example, a major factor in the miniaturization of computer chip lithography – the very short wavelength of deep UV light allows for focusing of a lithographic beam down to just a few dozen nanometers. However, for many imaging applications, such as the observation of biological samples, even near ultraviolet light is damaging due to the higher photon energy compared with visible wavelengths.

No practical lens or objective can achieve ϕ greater than 90° (with the technical exception of a 4π microscope). So, the only remaining option to improve resolution is to change the surrounding medium to a high-index material (higher than the default, air). For this reason, water immersion and oil immersion microscope setups are very popular with biologists and other scientists who require high resolution optical imaging. But even this approach offers limited improvement. To achieve a *NA* of 1.6, special oil and expensive sapphire objectives are required. A *NA* of 2 is not considered practically achievable. So where does that leave us? A quick calculation can give an approximate value for diffraction-limited resolution at visible frequencies, even in a best-case scenario:

$$\delta = (0.61)(400\,\text{nm})/1.6 = 153\,\text{nm} \tag{1.5}$$

There are many active areas of research that are currently held back by imaging resolution. One of the most compelling, but far from the only area, is biological imaging. To observe a living cell and record the dynamics of sub-cellular components requires a non-invasive, non-damaging imaging technique with speed on the order of cellular dynamics, as well as resolution far below 100 nm. At present, there is simply no technique offering this combined performance at a satisfactory level. If such a technique can be realized, there is immense potential for discovery and new understanding.

1.2 Structured illumination microscopy

In recent years, many creative methods have been proposed and demonstrated to circumvent the diffraction limit. For fluorescent imaging, one of the most successful to date has been structured illumination microscopy (SIM), first proposed in 2000 by Gustafsson [Gus00]. Fig. 1.3 illustrates the core concept of this technique.

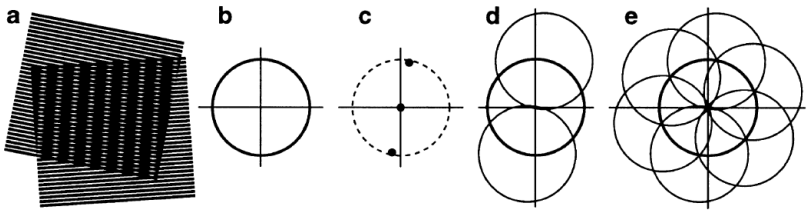

Figure 1.3: SIM concept: (a) Two line patterns representing an object and an illumination pattern are overlaid. (b) In Fourier space, diffraction limits the observable region to a circular area around the origin, known as the optical transfer function (OTF) of a microscope. (c) A positive-valued sinusoidal illumination pattern has just three Fourier components. If the sinusoidal pattern itself has diffraction-limited periodicity, then those components will be located as shown. (d) The imaging process under this structured illumination results in collected wavevectors from outside of the normal OTF, which can be used to reconstruct a super-resolved image. (e) To get uniform 2D super resolution, the pattern must be translated in multiple orientations, to fill up the larger effective OTF evenly. [Gus00]

Most real objects have a very broad spatial frequency spectrum. When we take a diffraction-limited image, we effectively throw away all the spatial frequency information outside of the OTF, resulting in an image with finite resolution. A key relation to understand here is the equivalence of convolution with the PSF in real space to multiplication in Fourier space. When an object is illuminated with a sinusoidal pattern rather than uniform light, the visible portion of the object is a multiplication in real space, and a convolution in Fourier space. The convolution creates shifted copies of the object information, such that information normally outside of the OTF will be brought into the observable region. The

shift magnitude is dictated by the spatial frequency of the illumination pattern. Several sub-images are required to create one full super resolution image from the combined pieces of spatial frequency (k-space) information.

Since a finer illumination pattern will allow us access to higher spatial frequency information, one might logically try to create as fine an illumination pattern as possible. In most SIM-based techniques, this pattern is created with a simple line-patterned grating. This and any other all-optical pattern-forming methods are naturally also diffraction-limited. Therefore, the maximum spatial frequency K of the pattern is equal to the maximum spatial frequency passed by a diffraction-limited OTF, and thus the resolution can be improved by a factor of two, at best. An example demonstration of experimental super resolution achieved by SIM is shown in Fig. 1.4. The imaged full width half maximum (FWHM) of the 120 nm beads is reduced, and the resolution is improved noticeably compared to the diffraction limit.

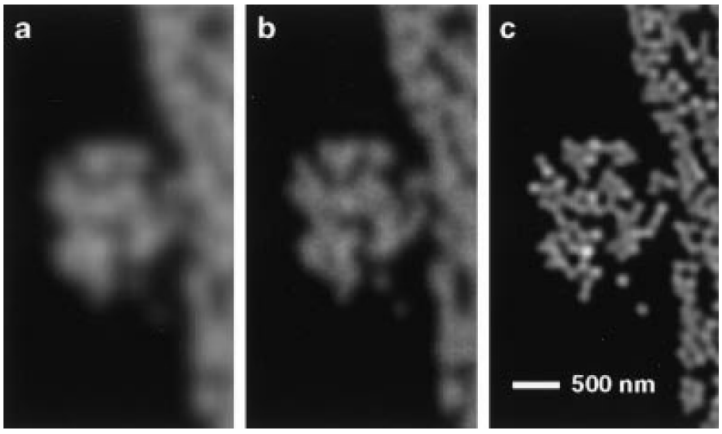

Figure 1.4: SIM imaging demonstration: A cluster of fluorescent beads with diameter = 120 nm, imaged by different methods. (a) Conventional microscope image (b) confocal microscope image. (c) SIM image, showing noticeably improved resolution. [Gus00]

The matter of piecing together the collected sub-images into a single super resolution

image is not a trivial task. It is not enough to simply collect high-k information at random; it must be captured and combined appropriately. Start with a basic imaging equation,

$$m_l(x,y) = [o(x,y)I_l(x,y)] * p(x,y) \tag{1.6}$$

where m is the recorded image, o is the object fluorophore density, I is the structured illumination pattern, and p is the point spread function. Note that all matrix "multiplication" here is actually the element-by-element Hadamard product, written with simplified notation for convenience. For a 1D sinusoidal illumination,

$$I_l(x,y) = 1 + \cos(2\pi Kx + \varphi_l) \tag{1.7}$$

where K is the spatial frequency of the illumination pattern, and φ is the phase of the pattern. The Fourier transform of Eq. 1.6 can then be written as

$$M_l(k_x,k_y) = \left[O(k_x,k_y) + \frac{1}{2}O(k_x+K,k_y)\mathrm{e}^{-i\varphi} + \frac{1}{2}O(k_x-K,k_y)\mathrm{e}^{i\varphi}\right] P(k_x,k_y) \tag{1.8}$$

In the above equation, the shifted copies of the object are apparent. Supposing three sub-images are recorded with the same 1D pattern shifted at three different phases, then we can represent a system of equations in matrix form,

$$\begin{bmatrix} M_1(k_x,k_y) \\ M_2(k_x,k_y) \\ M_3(k_x,k_y) \end{bmatrix} = \begin{bmatrix} 1 & \frac{1}{2}\mathrm{e}^{-\varphi_1} & \frac{1}{2}\mathrm{e}^{\varphi_1} \\ 1 & \frac{1}{2}\mathrm{e}^{-\varphi_2} & \frac{1}{2}\mathrm{e}^{\varphi_2} \\ 1 & \frac{1}{2}\mathrm{e}^{-\varphi_3} & \frac{1}{2}\mathrm{e}^{\varphi_3} \end{bmatrix} \begin{bmatrix} O(k_x,k_y)P(k_x,k_y) \\ O(k_x+K,k_y)P(k_x,k_y) \\ O(k_x-K,k_y)P(k_x,k_y) \end{bmatrix} \tag{1.9}$$

And defining the matrix A as

$$A = \begin{bmatrix} 1 & \frac{1}{2}e^{-\varphi_1} & \frac{1}{2}e^{\varphi_1} \\ 1 & \frac{1}{2}e^{-\varphi_2} & \frac{1}{2}e^{\varphi_2} \\ 1 & \frac{1}{2}e^{-\varphi_3} & \frac{1}{2}e^{\varphi_3} \end{bmatrix} \tag{1.10}$$

This system of equations can be rewritten as

$$\begin{bmatrix} O(k_x,k_y)P(k_x,k_y) \\ O(k_x+K,k_y)P(k_x,k_y) \\ O(k_x-K,k_y)P(k_x,k_y) \end{bmatrix} = A^{-1} \begin{bmatrix} M_1(k_x,k_y) \\ M_2(k_x,k_y) \\ M_3(k_x,k_y) \end{bmatrix} \tag{1.11}$$

And so we are left with a system of three equations and three unknowns, $O(k_x,k_y)P(k_x,k_y)$, $O(k_x+K,k_y)P(k_x,k_y)$, and $O(k_x-K,k_y)P(k_x,k_y)$, which can be solved easily. The ideal phase shift of the pattern between each sub-image is $\Delta\varphi = 2\pi/3$, so that the entire object plane will be evenly illuminated in total. Now that we have separated the image information into each of the three copies created by our illumination pattern, we can shift the high-k components into their proper places, and take the inverse Fourier transform to recover a super-resolved, real space image of the object. The mathematical process described above only results in super resolution along one direction. To achieve even, consistent super resolution in two dimensions, this process must be repeated with the pattern oriented in at least two directions, preferably three or more.

1.3 Plasmonics

Plasmonics is the study of the interaction between an electromagnetic field and the free electrons in a metal. The free conduction band electrons in a metal behave as a plasma and can be excited by the electronic component of light to undergo collective

oscillations. A plasmon is a quantum of plasma oscillation, just as phonons are quantizations of mechanical vibrations. In an undamped approximation, a plasmon oscillation in response to a displacement can be derived [Nov06] from a simple mass-and-spring model,

$$\omega_p = \sqrt{\frac{ne^2}{m_e \varepsilon_0}} \tag{1.12}$$

where ω_p is the plasma frequency, n is the conduction electron density, e is the elementary charge, m_e is the electron mass, and ε_0 is the free space permittivity. A periodic electric field displaces an electron, with an associated dipole moment

$$\mathbf{p} = e\mathbf{r} \tag{1.13}$$

where $\mathbf{p}$ is the dipole moment, and $\mathbf{r}$ is the displacement of the electron. In a real material possessing many free electrons, the polarization per unit volume $\mathbf{P}$ can be written as

$$\mathbf{P} = n\mathbf{p} \tag{1.14}$$

From the constitutive relations of Maxwell's equations we know that

$$\mathbf{P}(\omega) = \varepsilon_0 \chi_e(\omega)\mathbf{E}(\omega) \tag{1.15}$$

where ω is the angular frequency, $\mathbf{E}$ is the electric field, and χ_e is the electric susceptibility, related to the frequency-dependent permittivity by

$$\varepsilon(\omega) = 1 + \chi_e(\omega) \tag{1.16}$$

The displacement and ultimately the permittivity can thus be found by solving the equation of motion for electrons influenced by an external field. A common approach to this problem is known as the Drude model [Dru00], which ignores all interactions other than electron-nucleus collisions. In this approximation, electrons may be imagined like pinballs, bouncing around amongst relatively stationary and much heavier positive ions (see conceptual illustration in Fig. 1.5).

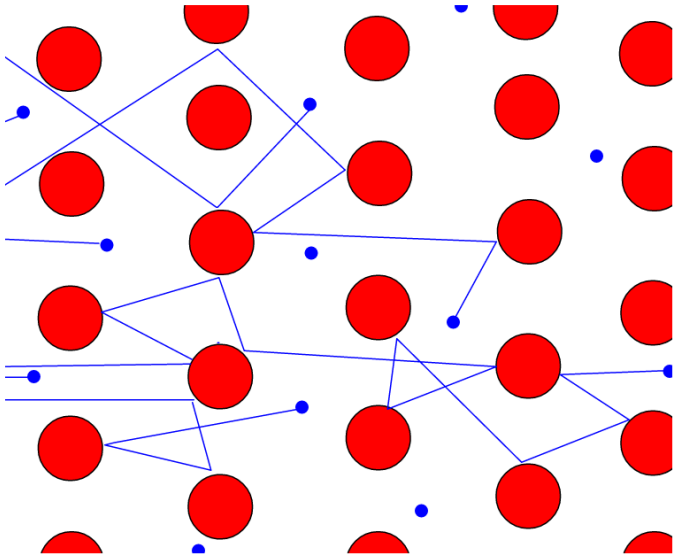

Figure 1.5: Drude model concept: Electrons (blue) collide with immobile positive ions (red). [Gar07]

We can write an equation of motion,

$$m_e \frac{\partial^2 \mathbf{r}}{\partial t^2} + m_e \Gamma \frac{\partial \mathbf{r}}{\partial t} = e\mathbf{E}_0 \mathrm{e}^{-i\omega t} \tag{1.17}$$

where Γ is a damping term and is proportional to the Fermi velocity, and inversely

proportional to the electron mean free path between collisions. Using

$$\mathbf{r}(t) = \mathbf{r}_0 \mathrm{e}^{-i\omega t} \tag{1.18}$$

we can derive the Drude permittivity

$$\begin{aligned} \varepsilon_D(\omega) &= 1 - \frac{\omega_p^2}{\omega^2 + i\Gamma\omega} \\ &= 1 - \frac{\omega_p^2}{\omega^2 + \Gamma^2} + i\frac{\Gamma\omega_p^2}{\omega(\omega^2 + \Gamma^2)} \end{aligned} \tag{1.19}$$

The frequency-dependent permittivity tells us a lot about the plasmonic behavior of a material. As an example, the complex permittivity of gold is shown in Fig. 1.6. When Re(ε) is negative, the index of refraction is also negative for a non-magnetic material, according to $n = \sqrt{\varepsilon\mu}$. For frequencies below ω_p, this unusual property leads to low penetration depth for light waves incident upon the surface of a plasmonic material. If Im(ε) is large, then losses become significant. We call the wavelength span where the plasma follows the Drude model the Drude regime. For gold, this is primarily towards the longer-wavelength end of the visible spectrum, into the infrared. For other metals such as silver or aluminum, this behavior is present for shorter wavelengths. If the photon wavelength is too short, these higher-energy waves can excite valence electrons, and thus constitutes an interband regime, increasing the loss, and making the Drude model inaccurate for this regime.

A surface plasmon polariton (SPP) is a quantum of surface charge density oscillation. These plasmonic modes, bound to the interface between a metal and a dielectric, arise as homogeneous solutions to Maxwell's equations when the metal has a large negative

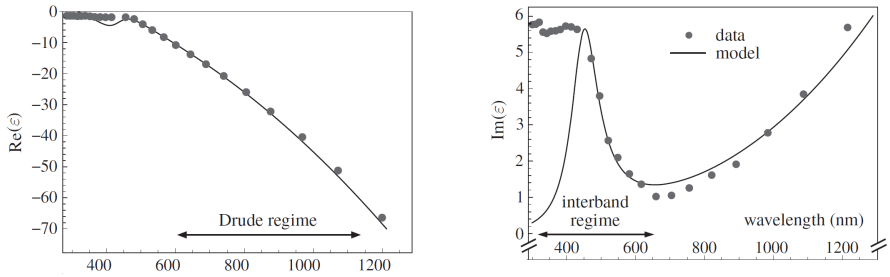

Figure 1.6: Optical permittivity of gold: Experimental data and theoretical curves showing the real (left) and imaginary (right) components of $\varepsilon(\omega)$ for gold in the optical regime. [Nov06]

permittivity ε_1, and the dielectric has a small positive permittivity ε_2. The dispersion relation in the propagation direction along the interface is

$$k_x^2 = \frac{\varepsilon_1 \varepsilon_2}{\varepsilon_1 + \varepsilon_2} \frac{\omega^2}{c^2} \tag{1.20}$$

In the low-loss approximation, we can write the real part of k_x (k_x') generated by p-polarized incident light as

$$k_x' \approx \sqrt{\frac{\varepsilon_1' \varepsilon_2}{\varepsilon_1' + \varepsilon_2}} \frac{\omega}{c} \tag{1.21}$$

Where ε' is shorthand for the real part of the permittivity. The SPP wavelength can then be calculated as

$$\lambda_{SPP} = \frac{2\pi}{k_x'} = \sqrt{\frac{\varepsilon_1' + \varepsilon_2}{\varepsilon_1' \varepsilon_2}} \lambda_0 \tag{1.22}$$

where λ_0 is the wavelength of the photon in free space possessing the same angular frequency. A quick examination of the above equation suggests that we will have access to shorter wavelengths compared to photons of the same frequency. A depiction of the SPP propagating along an interface is shown in Fig. 1.7. Due to loss, most SPPs have a

propagation length of less than 50 μm before losing most of their field strength.

Because the SPP phenomenon is inherently confined to the interface, it exhibits evanescent exponential decay in both directions perpendicular to the propagation direction. Fields are typically negligible at distances greater than 300 nm into the dielectric, and at just 25 nm into the metal. This confinement of the electric field enhances the local field strength.

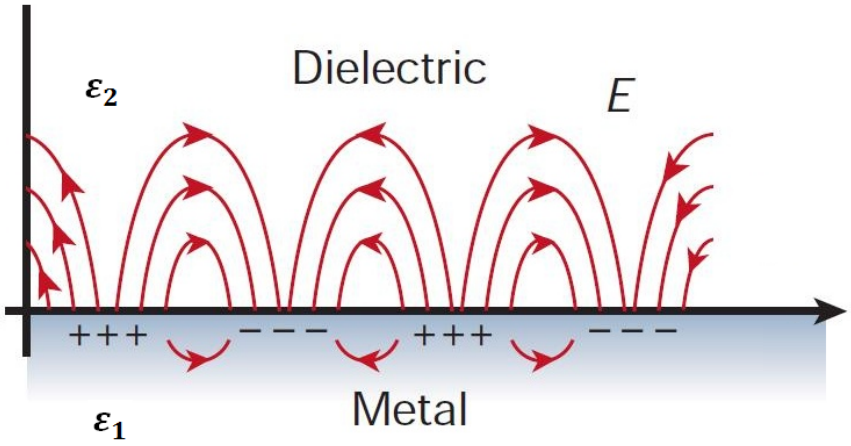

Figure 1.7: Surface plasmon polariton concept: This schematic depicts the interaction between an electric field and the free electrons present in a SPP. [Deu16]

Of course, an SPP is not automatically generated whenever light at the right wavelength hits a metal. Just as a dispersion curve exists relating ω to k for a photon, a SPP mode has its own dispersion curve, as approximated by Eq. 1.21. For a photon to "jump" from free-space propagation into a bound SPP mode with a shorter wavelength, some momentum transfer must be provided so that the total momentum is conserved. This can be accomplished in a variety of ways using gratings, prisms, or other mechanisms.

Another variety of plasmonic excitation is called a localized plasmon (LP). As their name suggests, a LP is always localized to some non-flat geometry, and does not propagate. LP modes arise as solutions to the homogeneous wave equation, where the local interface geometry facilitates a restoring force for free electrons driven by an oscillating

field. Radiative by nature, LPs can couple to propagating radiation without any additional mechanism. Perhaps the simplest type of LP mode is a dipole mode, illustrated in Fig. 1.8, but higher-order modes can also exist (quadrupole, etc).

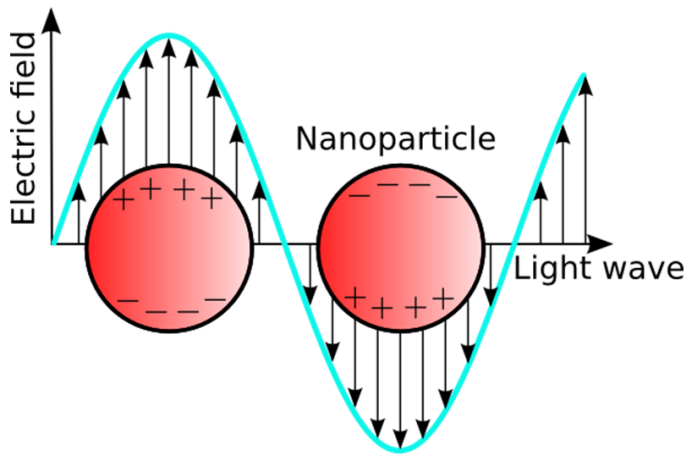

Figure 1.8: Localized plasmon concept: This schematic shows the interaction between the electric field and free electrons present in a LP mode for a spherical nanoparticle. [Uni13]

The LP modes of small metallic particles have a resonant frequency dependence, influenced by particle size and shape. In general, smaller geometries will be resonant at shorter wavelengths. The particles or features hosting a LP mode must necessarily be small relative to the wavelength of light in at least one dimension, in order that the electric field affects the entire geometry strongly. The resonance is strongly affected by the complex permittivity of the metal as well as that of the surrounding medium. Due to material differences, silver particles typically have strong plasmonic responses at the short end of the visible spectrum, while gold particles are more strongly plasmonic at longer wavelengths. In most cases, a surrounding medium with a higher permittivity will cause a redshift in the plasmonic response.

Chapter 2

Localized plasmonic structured illumination microscopy theory

A new super resolution imaging method, i.e. localized plasmon assisted structured illumination microscopy (LPSIM), is introduced in this chapter. LPSIM uses an array of localized plasmonic antennas to provide dynamically tunable near-field excitations resulting in finely structured illumination patterns, independent of any propagating surface plasmon dispersion limitations. The illumination pattern feature sizes are limited only by the antenna geometry, and a far-field image resolved far beyond the diffraction limit is obtained. This approach maintains a wide field of view and the capacity for a high frame-rate. The recovered images for various classes of objects are presented, demonstrating a significant resolution improvement over existing methods.

2.1 Physical principles of LPSIM

The use of optical microscopes has had a profound impact in the field of biology for many decades. Visible light is generally safe and will not damage a living sample at reasonable intensities. As biologists have delved deeper into the study of living structures, however, the demand has increased for live images with resolution on the scale of cellular organelles and beyond. Unfortunately, the wave-particle duality of light places a fundamental limit on the spatial resolution achievable for a given illumination wavelength. This is known as the Abbe diffraction limit, and states that the smallest resolvable distance d between two objects is about $d = \lambda/2NA$, where NA is the numerical aperture of the objective, and λ is the wavelength of the light illuminating the sample. This leads to a maximum imaging resolution of approximately 200 nm for visible light. High-energy, short-wavelength probes such as X-rays or electrons can indeed provide additional imaging detail, but these methods are inherently harmful to most organic samples.

With the increasing demand for high resolution using visible light, many novel microscopy techniques have been proposed and shown experimentally in recent years. These methods include single molecule localization [RBZ06][BPS$^+$06], stimulated emission depletion microscopy (STED) [HW94][DH02], near-field scanning optical microscopy (NSOM) [AN72][PDL84], the far-field superlens (FSL) [DLSZ06][LDL$^+$07][XLSZ07], the hyperlens [SE06][LLX$^+$07b], the metamaterial immersion lens (MIL) [ML10], structured illumination microscopy (SIM) [HC99][HC99][SCH$^+$08][HJC02][Gus05], plasmonic structured illumination microscopy (PSIM) [WL10], and others [GZF05][SCB06]. Although these methods have found successful application in laboratories and as commercial equipment, each has its respective limitations.

For high-resolution, high-speed, *in vivo* imaging, SIM has proven especially use-

ful. The optical transfer function (OTF) of a standard, diffraction-limited epifluorescence microscopy setup can be represented by a circle with a radius determined by the cutoff frequency $k_{cutoff} \cong 2NA/\lambda$ (see the central circles in Fig. 2.1). SIM uses Moiré fringes to bring high-frequency information into the detectable regime, thus improving the image resolution [KBL96]. This process can be described in real space and frequency space by the following equations,

$$m(\mathbf{r},\varphi) = \{o(\mathbf{r})[1+\cos(Kx+\varphi)]\} * p(\mathbf{r}) \tag{2.1}$$

$$M(\mathbf{k},\varphi) = P(\mathbf{k})\left\{O(\mathbf{k}) + \frac{1}{2}[e^{i\varphi}O(\mathbf{k}+\mathbf{K}) + e^{-i\varphi}O(\mathbf{k}-\mathbf{K})]\right\} \tag{2.2}$$

where m is the recorded image, o is the actual object, p is the point spread function (PSF) of the microscope, and $1+\cos(Kx+\varphi)$ represents an example structured illumination pattern, with spatial frequency K and phase φ. As can be seen from the above equations, this imaging process provides information outside the standard OTF. Several sub-images are collected with different pattern phases and orientations, and a full super-resolved image is reconstructed. This method has proven remarkably successful, although its illumination patterns are still inherently limited by diffraction. This leads to a two-fold resolution improvement (Fig. 2.1(a)) compared to conventional epifluorescence microscopy, with a best-case resolution of approximately 100 nm for visible illumination wavelengths. Several new methods have been proposed, such as saturated structured illumination microscopy (SSIM), and random speckle illumination [MBG$^+$12]. However, these methods have significant drawbacks including fluorescent bleaching, slow imaging speed, and a high number of sub-images required.

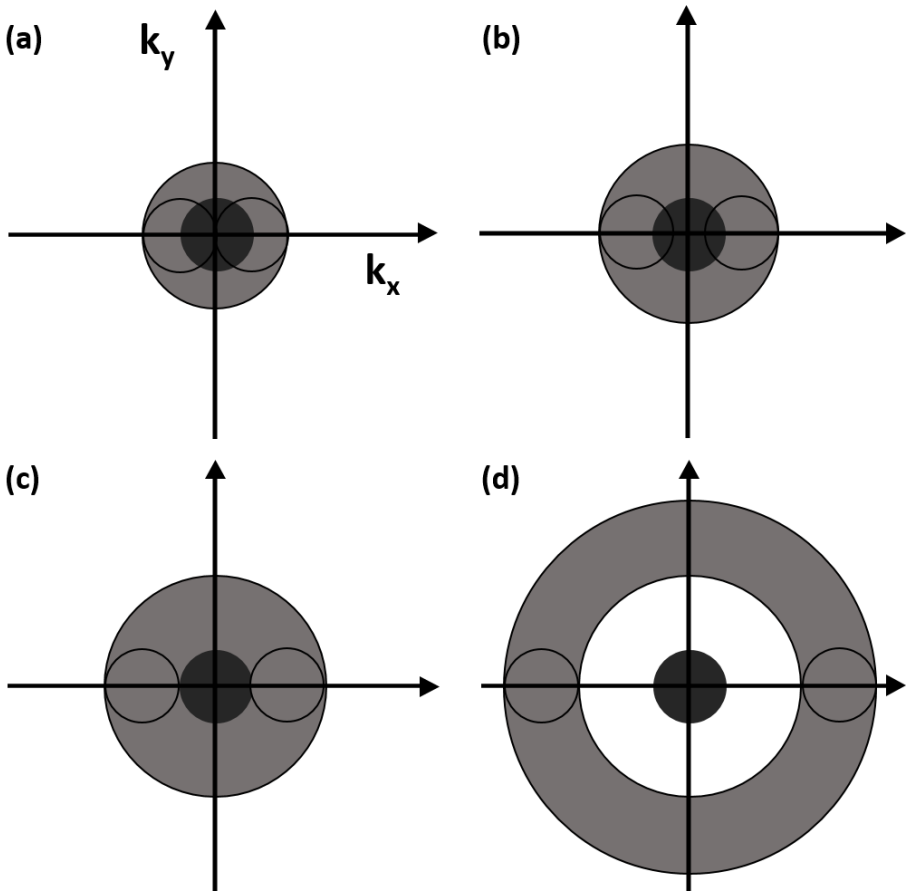

Figure 2.1: *k*-space illustration of resolving power: The dark central circle represents the spatial frequencies detectable with a diffraction-limited imaging setup. (a) OTF of the SIM technique. (b) PSIM OTF. (c),(d) Two potential LPSIM schemes using excitation patterns with large *k*-vectors, dramatically enhancing resolving power.

In this letter, we propose a novel, deeply sub-diffraction optical imaging technique called localized plasmon assisted structured illumination microscopy (LPSIM), which uses localized plasmons (LPs) generated on an antenna array in concert with reconstruction methods based on known illumination patterns to significantly improve resolving power (two potential OTFs shown in Fig. 2.1(c),(d)). We will describe in detail the physical principles of LPSIM, and then show an example numerical demonstration of the performance of the proposed method. Advantages and disadvantages of this technique will also be discussed.

Localized plasmon resonances are physically understood as collective electron charge oscillations in metallic structures, excited by incident electromagnetic radiation [Rae88]. These phenomena have been studied at length, and have found practical use in a wide range of fields [NLL82][JVD77][AC77][Mos85][GSC$^+$12][GAJ$^+$13][LCS$^+$09]. With recent advances in nanoscale fabrication techniques, controlling electric fields at nanoscale has become a valuable tool. Because LPs are fundamentally bound to the metal-dielectric interfaces they inhabit, their size is determined primarily by the geometry of the interface. LPSIM takes advantage of this characteristic, utilizing plasmonic excitations on a 2D array of LP antennas, which serve as structured illumination patterns. These patterns, unlike those of SIM or PSIM, can have almost arbitrary spatial frequency, so the spatial resolution obtainable with this method is not fundamentally limited by free-space or propagating surface plasmon polariton dispersion relations (See Fig. 2.2(g)). This allows us to collect *k*-space information from arbitrary regions based on the LP antenna array design. In this letter, we place our LPSIM *k*-ring as shown in Fig. 2.1(c), for a 3X resolution improvement over standard microscopy.

Our antenna design and illumination scheme is described below, and is shown in Fig. 2.2. The silver nano-antennas are 60 nm in diameter with a one-to-one aspect

ratio. They are spaced 150 nm apart (center to center). They are surrounded by a glass dielectric. The hexagonal array structure (See schematic in Fig. 2.2(a)) has 3-fold rotational symmetry, allowing us to scan our plasmonic pattern in three orientations to collect the full Fourier information. Changes to the plasmonic pattern were controlled by the incident illumination angle, and resulted in tunable excitations, as shown in Fig. 2.2(b)-(f). CST Microwave Studio frequency domain finite element solver was used to numerically simulate the electromagnetic field distributions in the object plane, with incident light of 405 nm. This excited the nanodiscs at a frequency near their dipole resonance. Silver permittivity was calculated by interpolating data [JC72]. The imaging calculations were handled analytically, with an Airy pattern PSF [Sha06].

The illumination pattern was recorded in a 2D plane 40 nm behind the nano-antenna array, where we placed our object. Twenty-one sub-images (3 incident planes $\times$ 7 incident angles) were used to fill in our *k*-space picture, as opposed to the typical 9 sub-images (3 pattern orientations $\times$ 3 pattern phases) used in SIM. For high speed imaging, fewer sub-images is preferred, but by adding additional incident angles we were able to improve image quality. The number of sub-images may be decreased with further design optimizations.

Despite our dispersion-independent excitation patterns, the incident wavelength matters for two reasons. For one, because the standard OTF is still limited by $k_{cutoff} = 2NA/\lambda$, the incident wavelength will affect our strategy for collecting high-spatial frequency details if we want to avoid "gaps" in our final *k*-space information. Specifically, if we take the approach of following the translation scanning scheme used in SIM, then the ideal K value would be $2k_{cutoff}$, since anything higher would result in a region of missing information between our standard OTF and our collected outer lobes. Our nano-antenna array had a pitch corresponding to $2k_{cutoff}$, which resulted in a tripling of the resolving

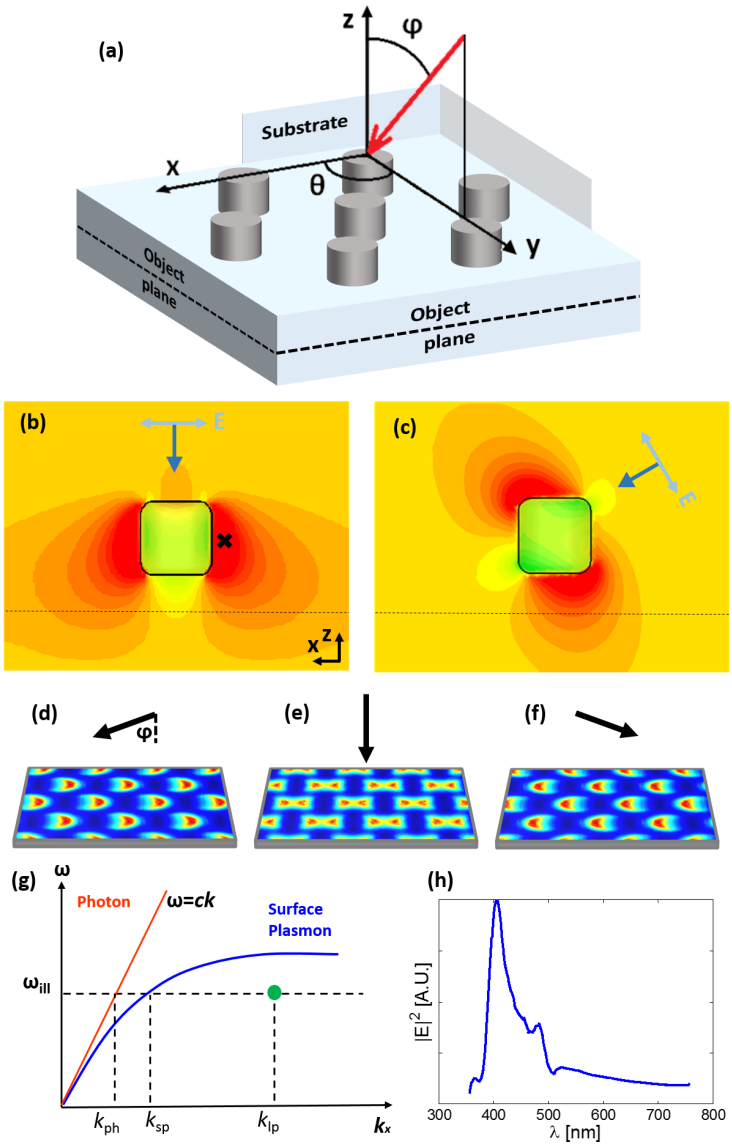

Figure 2.2: Proposed imaging scheme: (a) schematic for LPSIM pattern translation. The red arrow represents p-polarized laser light, directed towards the plasmonic substrate at varying angles to create near-field excitation patterns a short distance behind the antennas, in the object plane. (b),(c) Field strength around a nanodisc excited by laser light at incident angles of $\theta = 0°$, $\varphi = 0°$ and $60°$, respectively. (d)-(f) Object plane patterns for incident angles $\theta = 0°$ and $\varphi = 60°$, $0°$, $-60°$ respectively, as used in reconstruction. (g) Dispersion advantage of LPSIM over existing methods. SIM and PSIM are limited by the red and blue dispersion curves, respectively. For LPSIM, the green dot shown is determined only by the antenna geometry. (h) Electric field magnitude at a fixed position (see the "x" in part *(b)*) for a single nanodisc under normally-incident illumination showing resonant behavior.

power compared with standard microscopy, and a doubling of the improvement gained by SIM. Secondly, the nano-antennas have a resonant LP frequency, so exciting them on or away from the resonance will affect the strength and features of the LPs.

Figure 2.2(h) shows the resonance curve for a single silver nanodisc under normally incident laser illumination. It bears mentioning that a disc presents a different profile to light incident from varied angles, so the localized plasmon spectrum will have some degree of angle dependence. An array of these discs will be subject to additional frequency dependence for a number of reasons, all of which contribute to the final optimized design geometry. For one, constructive interference in the array leads to a sharpening and enhancement of the resonance [HZS$^+$05], and this interference condition changes with the incident angle [KSG08]. Additionally, in a densely packed periodic array, overlap of evanescent fields between adjacent particles can de-phase and reduce the amplitude of the plasmon excitation [FWMDN09].

2.2 Image reconstruction

Because the illumination patterns available to LPSIM are not perfectly sinusoidal, the classic SIM image reconstruction math cannot be used without some adaptation. However, by taking an alternative approach [GZF05], we can simplify things a great deal. By using what we will call a delta-sampling reconstruction method, we remove the requirements of strictly translated sinusoidal patterns, and are able to reconstruct a super resolution image using the set of LP field excitations.

We can think of the plasmonic excitation patterns as high resolution masks projected onto the object. Just as it happens in standard SIM, this allows for the capture of high-k information with diffraction-limited far-field optics. The key is in how this information is

reconstructed. Each image taken involves low-pass filtering of the object which is described in real space by convolution with the PSF,

$$m_{\xi}(\mathbf{r}) = [o(\mathbf{r})I(\mathbf{r}-\xi)] * p(\mathbf{r}) = \int [o(\mathbf{r}')I(\mathbf{r}'-\xi)]p(\mathbf{r}-\mathbf{r}')\mathrm{d}\mathbf{r}' \tag{2.3}$$

where ξ is the shift in the pattern, effected in this case by changing the incident laser angle to the nano-antenna array. If we collect a series of images with different shifts, multiply the images with the known illumination patterns, and add them together, we have

$$\begin{aligned} m(\mathbf{r}) &= \int\int \{[o(\mathbf{r}')I(\mathbf{r}'-\xi)]p(\mathbf{r}-\mathbf{r}')\}I'(\mathbf{r}-\xi)\mathrm{d}\mathbf{r}'\mathrm{d}\xi \\ &= \int m_{\xi}(\mathbf{r})I'(\mathbf{r}-\xi)\mathrm{d}\xi \end{aligned} \tag{2.4}$$

Now if we define a convenient parameter,

$$\tau(\mathbf{r}-\mathbf{r}') = \int I(\mathbf{r}'-\xi)I'(\mathbf{r}-\xi)\mathrm{d}\xi \tag{2.5}$$

then we can rearrange terms to write

$$\begin{aligned} m(\mathbf{r}) &= \int o(\mathbf{r}')p(\mathbf{r}-\mathbf{r}')\tau(\mathbf{r}-\mathbf{r}')\mathrm{d}\mathbf{r}' \\ &= \int o(\mathbf{r}')p'(\mathbf{r}-\mathbf{r}')\mathrm{d}\mathbf{r}' \\ &= o(\mathbf{r}) * p'(\mathbf{r}) \end{aligned} \tag{2.6}$$

where we define p' as the effective PSF of the full imaging reconstruction process,

$$p'(\mathbf{r}) = p(\mathbf{r})\tau(\mathbf{r}) \tag{2.7}$$

The function τ is the autocorrelation of the illumination pattern mask, as defined in Eq. (2.5). This autocorrelation will have a strong peak at the origin. Importantly, the width of this autocorrelation peak will be narrower than the PSF, because it is determined by the LPSIM field size, which is much smaller than the illumination wavelength. Therefore, the function p' can be approximated as a delta function,

$$p'(\mathbf{r}) \cong p(\mathbf{r})\delta(\mathbf{r}) = p(0)\delta(\mathbf{r}) \tag{2.8}$$

Finally, we can see that the resolution of our reconstruction image will be dependent on how finely we can structure our illumination patterns. Fortunately in the case of LPSIM, we can get very tightly confined patterns from localized plasmons, and thus we achieve super resolution.

2.3 Numerical imaging results

To demonstrate the effectiveness and robustness of the method described above, we tested the performance for the case of a single point particle, a distribution of quantum dots, and a non-sparse object with varying feature sizes. These objects were placed 40 nm behind the back edge of the nano-antenna array, where they were subjected to the near-field patterns generated by the LP excitations. For these simulations, we used fluorescent objects, with an emission wavelength of 430 nm. We assumed that the LP field intensity was in the linear regime of the fluorophore. Furthermore, we assumed that the objects themselves would not

dramatically affect the LP fields. The fluorescent emission is controlled by the LP-generated near-field patterns, but to be clear, the actual recorded image is captured in the far-field. Near-field, high *k*-value information is recovered and incorporated into the image during the reconstruction post-processing.

One of the most common ways to characterize the resolution of an imaging technique is with point particles. For this reason, we looked at the full width half maximum (FWHM) and two-point resolution of our technique using 5 nm quantum dots as our object. Shown in Fig. 2.3(a) is the standard, diffraction-limited image of a single quantum dot. This is effectively the PSF of the standard system. By comparison, Fig. 2.3(b) shows the image (or PSF) using the LPSIM technique. As can readily be observed, there is a marked improvement in resolution. Some asymmetry is introduced, in the form of weak circular artifacts surrounding the central spot. This is a result of an antenna design which maximizes resolution by positioning the high-frequency *k*-space lobes just on the edge of the standard OTF (Fig. 2.3(c)). This results in some small gaps in our overall k-space information, but it allows us to achieve excellent resolution with only minimal sacrifice in image quality, much of which can be eliminated in post-processing if necessary. Fig. 2.3(d) shows a profile across the x-axis of Fig. 2.3(a),(b), and from this graph we determine the FWHM. For the standard image, if we assume an oil-immersion *NA* of 1.4, the FWHM is 153 nm. For the LPSIM image, again with a *NA* of 1.4, the FWHM is reduced 3-fold to 52 nm. This is a dramatic improvement that surpasses the expected performance of both SIM [Gus00] and metal-dielectric PSIM. No deconvolution is used to enhance this result, although in many relevant specific cases, deconvolution or other numerical processing of the LPSIM image will allow for additional improvement in image quality. It should be noted that some asymmetry is present in our curves due to position-dependent distortion introduced by

imperfectly controllable excitation patterns. Another test of resolving power is the Rayleigh criteria [Won01]. This can be approximated by observing the distance at which two point particles are separated by a 30% intensity dip. As shown in Fig. 2.3(e), two quantum dots spaced 51 nm apart are totally unresolvable with a standard epifluorescence setup. With the LPSIM approach, however, we observe a 30% dip, as expected. This confirms our goal of a 3-fold improvement over the standard image resolution.

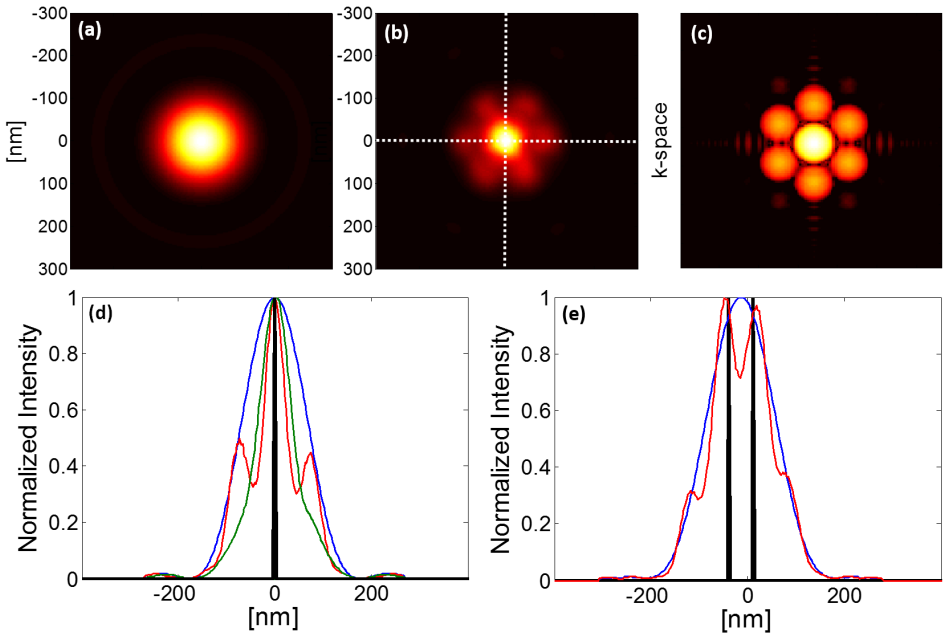

Figure 2.3: Resolution characterization: PSFs of (a) a diffraction-limited system, and (b) the LPSIM technique. (c) Expanded OTF after LPSIM reconstruction. Note that the six lobes surrounding the central region are high-frequency information captured by LPSIM. (d) FWHM comparison of diffraction-limited [blue] and LPSIM [red] techniques, for fluorescent emission at 430 nm. The green curve shows the FWHM taken along the vertical line in *(b)*. (e) Two-point resolution. For two 5 nm quantum dots placed 51 nm apart, a standard setup [blue] will not resolve the points, but with LPSIM [red], the typical Rayleigh criteria of a 30% intensity dip is satisfied.

While a point particle is useful for measuring FWHM and testing the Rayleigh criteria, many practical objects of interest to biologists and others are more complex. For this reason, we show results for a distribution of many quantum dots, including several

that are clustered together. Fig. 2.4(a) shows the standard image of such an object, and Fig. 2.4(b) shows the LPSIM-recovered object. By normalization of the collected image's frequency-domain magnitude to a generally expected magnitude envelope, a clean, highly resolved image is obtained, shown in Fig. 2.4(c). As can be seen by examination, in addition to a sharpening of single point particles, several unresolved clusters of quantum dots have been resolved into separate points by our LPSIM method. The dot distribution is more general than a single quantum dot, but it is still a sparse object. We also tested a non-sparse converging stripe object (Fig. 2.4(d)), which was chosen for its varying feature size as a visual demonstration of resolving power. Fig. 2.4(e),(f) show the standard and LPSIM images, respectively. Clearly, the diffraction-limited image is completely unresolved in the central region, whereas the LPSIM image reveals the converging stripes deep in towards the center of the object. These objects are shown as examples, but the LPSIM method will be useful for a wide variety of object types.

Like other existing methods, LPSIM has its strengths, but it is not without its disadvantages. Silver as a material choice has drawbacks due to oxidation issues, while gold has a resonance at longer wavelengths, making small geometry arrays inefficient. Although LPSIM is a far-field imaging technique, it relies on near-field LP excitation to induce the fluorescent emission, so any object of interest must be within $\sim$100 nm of the metallic substrate in order for the near-field to have sufficient strength [WE79][DKF$^+$02]. However, this limitation can at times be useful if one wishes to probe only the surface of a sample, without interference from layers at other depths. In a well-designed experiment, quenching and bleaching effects are negligible further than 20 nm from the LP source [Bar98]. In a LPSIM experiment, accurate antenna simulation, fabrication, and alignment will be important for a reconstruction based on known illumination patterns. Careful design

and optimization of the nano-antennas and the incident light polarization is needed, because getting effective pattern translation is difficult with fields confined to a fixed geometry. This limitation in illumination pattern flexibility leads to the irregularities seen in Fig. 2.4(c),(f). Fortunately, these problems can be minimized by careful design and reconstruction.

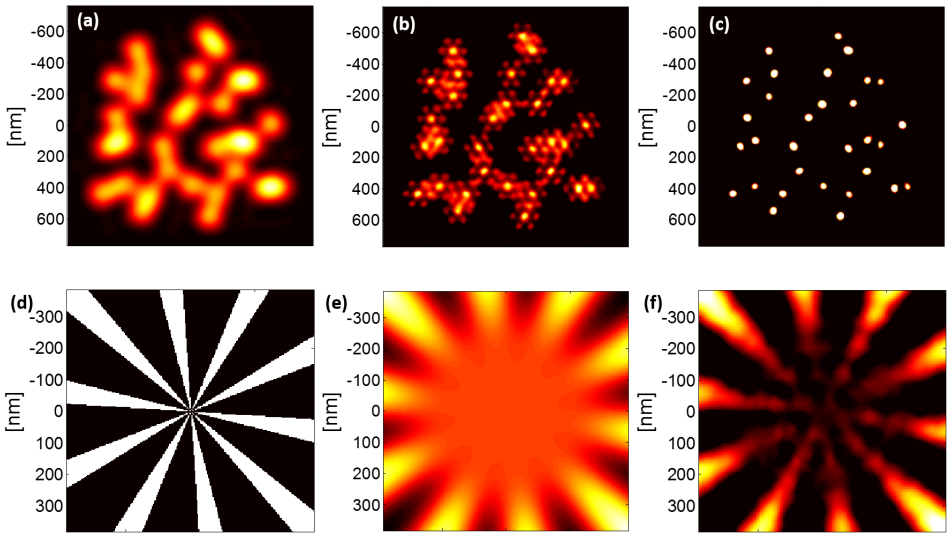

Figure 2.4: Imaging results: (a) Diffraction-limited image of a distribution of 5 nm-diameter fluorescent quantum dots. (b) LPSIM image of the same object. Previously unresolvable points are resolved. (c) Additional Fourier-based deconvolution combined with LPSIM yields a clean, highly resolved image. (d) A solid striped object. (e) Diffraction-limited image. (f) LPSIM image. The stripes are now resolvable much further in towards the center of the image.

To reiterate, there are a number of advantages to the proposed LPSIM method in comparison with the various existing methods. In point-scanning techniques, if a large field of view relative to the scanning point size is desired, the imaging speed will be slow since the point must scan across the entire plane to reconstruct a single full image. In our method, we translate known, non-sparse excitation patterns in a strategic manner, to collect the information for many locations in parallel, enabling a large field of view without sacrificing speed. Our method is also scalable; for different incident wavelengths the same 3-fold

resolution improvement could be achieved by resizing the antennas and the pitch of the array to appropriately position the *k*-space collection region. The expected imaging speed is similar to that of SIM [FSR$^+$12], with a comparable number of sub-images required to capture each full frame. And to re-emphasize, this method allows us to design illumination patterns with deep sub-wavelength features, regardless of the photonic dispersion curve. The *k*-space region collected by LPSIM is confined only by fabrication limitations. In fact, in cases such as certain dark-field microscopy setups [KCN$^+$10] only very high-*k* information is relevant. Our method could be used in these situations with even smaller geometry to achieve greater than 3-time resolution improvement. Furthermore, a cleverly designed substrate could be used with multiple feature sizes or a quasi-periodic structure, each excited by a different illumination wavelength. This strategy could be employed to collect information from a larger area in *k*-space and further enhance resolution. Besides experimental demonstration of this concept, further work could include a combination of PSIM and LPSIM, utilizing the high *k*-vector of LPSIM in concert with the pattern flexibility of PSIM to make smoother field patterns, allowing for better pattern control. This would allow for high-quality, high-speed, high-resolution imaging. Lastly, designing an antenna with a resonance peak at the incident wavelength enhances fluorescence and reduces the required exposure time.

In conclusion, we have demonstrated a new technique for super resolution imaging, named localized plasmon assisted structured illumination microscopy (LPSIM). Our numerical results have shown a resolution improvement larger than that expected from SIM or PSIM, without resorting to high intensity light and the nonlinear response of fluorescence emission subject to such light. The objects we have imaged in this paper consistently show a cleanly resolved 3-fold improvement over conventional epifluorescence microscopy. In

the future, LPSIM may find useful application in many biological and biomedical fields of research, especially among researchers interested in taking live video of cellular dynamics.

Chapter 2, in part, is a reprint of the material as it appears in Nanoscale, 2014, 6, 5807-5812. Joseph L. Ponsetto, Feifei Wei, Zhaowei Liu, “Localized plasmon assisted structured illumination microscopy for wide-field high-speed dispersion-independent super resolution imaging”. The dissertation author was the first author of this paper.

Chapter 3

Experimental demonstration of LPSIM

In recent years, surface imaging of various biological dynamics and biomechanical phenomena has seen a surge of interest [Axe01][MTH12][CSP+13]. Imaging of processes such as exocytosis [SGAS00] and kinesin motion [LKW+03] are most effective when depth is limited to a very thin region of interest at the edge of the cell or specimen. However, many objects and processes of interest are of size scales below the diffraction limit for safe, visible wavelength illumination. Super-resolution imaging methods such as structured illumination microscopy [Gus00][KSS+10] and others [RBZ06][LL12][WHMH07] have offered various compromises between resolution, imaging speed, and bio-compatibility. Here we report a new experimental technique which offers advantages over existing methods. Using finely structured, resonant, and controllable near-field excitation from localized surface plasmons, we achieve wide-field surface imaging with resolution down to 75 nm while maintaining reasonable speed and compatibility with biological specimens.

3.1 LPSIM imaging setup

Since Ernst Abbe described the diffraction limit over a century ago, high resolution optical imaging has become increasingly limited by the fundamentally diffractive nature of the illumination used to obtain an image. Many creative methods to circumvent this limitation have been developed, such as structured illumination microscopy (SIM) [Gus00][KSS+10], stochastic optical reconstruction microscopy (STORM) [RBZ06], the hyperlens [LL12][WPLon], stimulated emission depletion (STED) [WHMH07], photoactivated localization microscopy (PALM) [BPS+06], and the far-field superlens (FSL) [LDL+07].

All of these methods have tradeoffs between several factors such as resolution, speed, field of view, bio-compatibility, sensitivity, and experimental complexity. Localization-based techniques such as STORM and PALM are typically slow, albeit with very high resolution. Other techniques such as STED and saturated SIM (SSIM) [Gus05] require strong intensities which can harm sensitive biological samples. Standard SIM has seen widespread adoption [SEG15] due to its combination of super-resolution, practicality, and reasonable imaging speed [KCG+09][SCH+08]. However, since the illumination structure in SIM is itself diffraction-limited, the resolution can only be improved about two-fold versus standard microscopy. Traditional SIM utilizing the best available optics is not enough to bring the resolution down to deep sub-100 nm scales [LSC+15], despite tremendous demand for such a tool in various applications.

It is always possible to improve resolution by decreasing the illumination wavelength. However, this is accompanied by an increase in photon energy, which becomes prohibitive for bio-samples even at ultraviolet frequencies. One approach with demonstrated success, plasmonic SIM (PSIM) [WL10][WLS+14], achieves shorter wavelength without increasing

the photon energy by taking advantage of surface plasmon polariton (SPP) [BDE03] dispersion at a metal-dielectric interface. The PSIM method has potential for higher resolution, if the dispersion properties can be specially designed and combined with traditional SIM [FDLP15].

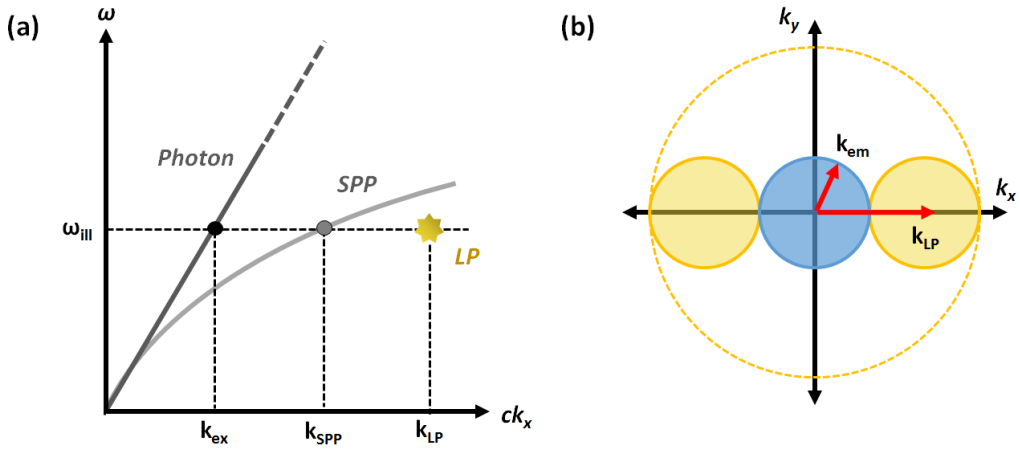

Figure 3.1: LPSIM conceptual overview: (a) Illustrative plot of temporal frequency versus wavenumber for the illuminating laser, the PSIM method (light gray curve), and the LP field (gold star) in an example LPSIM experiment. Here, k_{LP} is the spatial frequency generated by the nano-antenna array, which can be tuned as desired, within fabrication capabilities. (b) Spatial frequency scheme: The collected wavevectors in a traditional image are limited by the emission wavenumber k_{em} (blue circle). With structured illumination via LP fields, this imaging resolution is enhanced dramatically in a controllable manner (gold dashed circle, in this specific example).

Taking the push for subwavelength imaging significantly further is a new technique, localized plasmonic SIM (LPSIM), demonstrated here in experiment for the first time. Rather than be confined to the energy-wavelength relation dictated by either photonic or SPP dispersion, we design a substrate which gives us controlled, tunable, ultrafine illumination patterns, untethered to any dispersion relation. This is accomplished using localized plasmons (LPs) generated by a nano-antenna array [PWL14]. Localized plasmons are bound to the local geometry of a metal-dielectric interface [WVD07], and thus do not

have a wavelength, strictly speaking. The spatial frequency of an array of LPs is therefore determined primarily by the local geometry itself, which can be designed arbitrarily and can be much larger than that of light or SPPs, as shown in Fig. 3.1(a).

The spatial frequency k of a pattern generated with LPs can thus be dramatically higher than the wavenumber of the fluorescent light which is collected to form the image. Images formed in the far-field will have diffraction-limited resolution, as shown by the blue circle in Fig. 3.1(b). Under structured illumination, the Moiré effect [OWZ64] transfers information from higher spatial frequencies into the observable regime of the diffraction-limited optical transfer function (OTF). With knowledge of the illumination structure and the point spread function (PSF) of the imaging system, this high-k information can be shifted back to its origin in Fourier space [GAS00], enabling super resolution. This concept is used in all SIM-based techniques. LPSIM is differentiated by the very fine structure enabled and dictated by a nano-antenna array through k_{LP}, which breaks the diffraction limit for propagating waves and allows for the collection of extremely high spatial frequency information. A combination of SIM, PSIM, and LPSIM could be used to fill in a very large effective OTF, and provide a 5X or more improvement in resolution over standard optics. However, the k_{LP} chosen in this proof-of-concept experiment was designed to yield a 3X resolution improvement over a diffraction-limited image, solely by LPSIM.

To generate changeable structured excitation patterns with LP fields, a 2D hexagonal array of silver nanodiscs was illuminated with a laser near the disc dipole resonance. The resulting plasmonic field patterns can be shifted in a controllable manner within the object plane by changing the incident angle and polarization of the laser [PWL14]. These fields excite fluorescent emission in a fluorescent tagged object (Fig. 3.2, inset).

Fig. 3.2 shows the schematics of the experimental LPSIM setup. The incident

angle is controlled by a 2D scanning mirror system in combination with a high numerical aperture (NA) 4f system. The achievable incident angle range in the setup was $\pm$ 56° in any incident plane. A cylindrical lens was used to account for the spatial offset of the first scanning mirror relative to the 4f system. Fluorescent emission was collected by a 1.2 *NA* 60X magnification water immersion objective, filtered, and passed through a tube lens for additional magnification. The images were recorded with an electron-multiplying charge-coupled device (EMCCD). Several lasers at various visible frequencies were aligned in parallel at the beginning of the optical path, to allow for easy switching based on the fluorescent dyes present in different objects.

The illumination lasers used for the images shown in this work were a Coherent OBIS 405 LX, and a Coherent Sapphire 488. The linearly polarized output laser light was passed through a quarter wave plate (QWP), providing circular polarization incident to a custom polarizer plate that passively picks out the desired in-plane polarization to pass to the nano-antenna array. The laser beam profile was cleaned using a pinhole placed in the Fourier plane between two lenses. The 2D scanning mirror system used was a Cambridge Technology MicroMax 673. A Zeiss Axioskop 2 microscope with motorized objective control was used for fluorescence imaging. Images were recorded with an Andor iXon 897 EMCCD, with 0.6 s exposure time. A dichroic beamsplitter and a band-stop emission filter were used to separate the fluorescent signal. A custom sample stage, translatable in three dimensions, was used to position the sample relative to the 4f system.

To ensure the proper polarization was used at all times during our 2D laser angle scan, a custom polarizer plate was designed (Fig. 3.3). Edmund Optics wire grid polarizer film was used due to a good compromise between power damage threshold, extinction ratio, and the practicality of cutting custom shapes out of the polarizer material. The polarizer

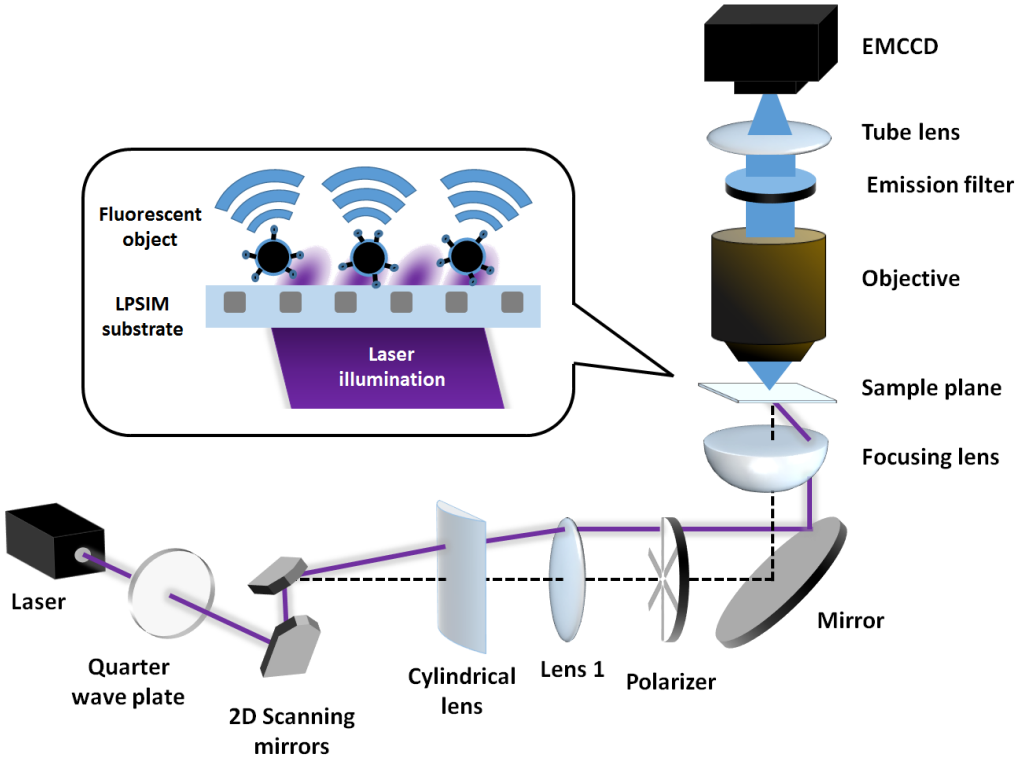

Figure 3.2: Schematic of the experimental imaging setup: An excitation laser is directed via 2D scanning mirrors through a high-NA 4f system which dictates the angle and plane of laser incidence to the nano-antenna array. In-plane polarization regardless of angle is guaranteed by a custom-made polarizer plate, which ensures the correct excitation patterns are formed. Emitted fluorescence is collected by the objective, filtered, and passed to the EMCCD. Inset: at the sample plane, fluorescent tagged objects are selectively excited by LP fields with fine-grained spatial dependence dictated by the nano-antenna geometry and the laser angle.

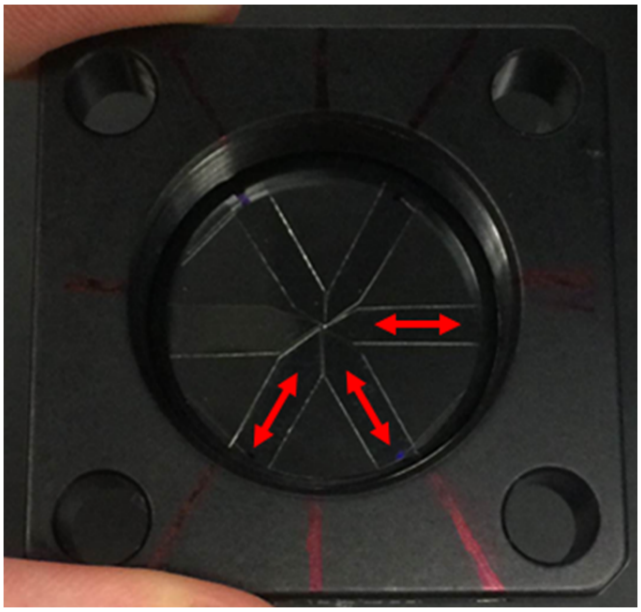

Figure 3.3: Custom polarizer plate: Strips of wire grid polarizing film were cut and placed as shown, with the allowed polarization direction indicated by the red arrows, along the length of the strips. This enabled us to passively maintain in-plane polarization while rapidly changing the incident laser angle within our 4f system.

was placed between the two lenses of our 4f system, where beam position corresponds to incident angle in the object plane. Exactly normal incident laser light was not used, as the beam was distorted by the polarizer edges at this angle. This polarization selection method inevitably causes insertion loss, but its passivity has the advantages of both simplicity and instantaneous response. Fig. 3.4 shows 9 example sub-images generated at different laser angles.

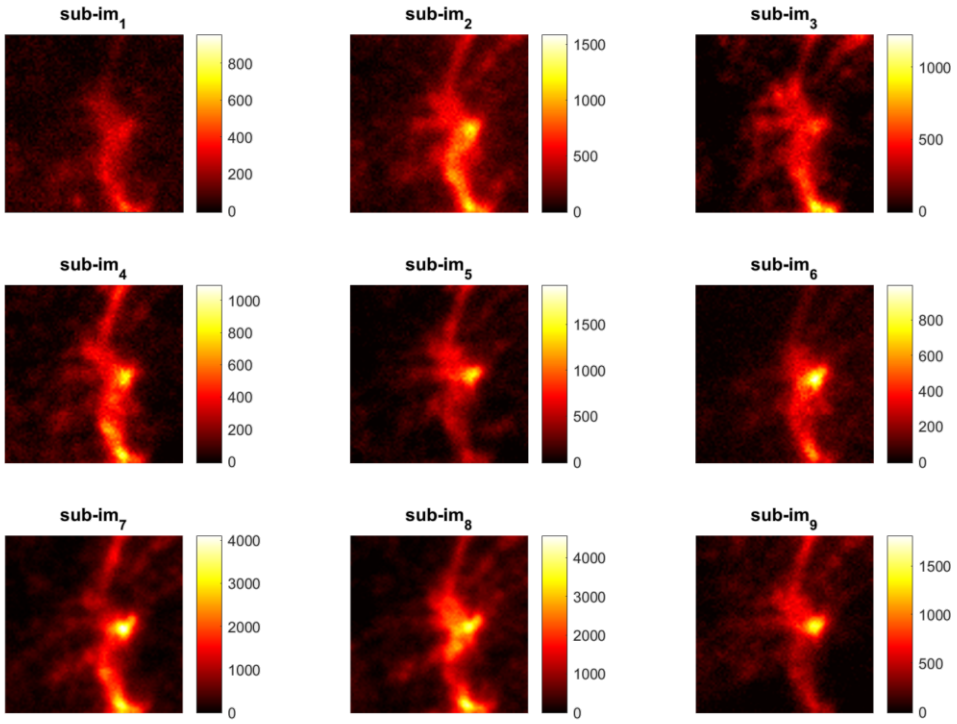

Figure 3.4: Example sub-images for reconstruction: For different laser angles, significantly different images are obtained. The scale bar is photon count (with electronic gain). The changing LP fields excite different areas of the object, resulting in nine different diffraction-limited images. The overall intensity varies for each plane of incidence, because the QWP is not perfectly aligned to generate circular polarization. In addition, the spot center moves somewhat for different laser angles due to various lens aberrations. Fortunately, much of this low-*k* intensity variation can be accounted for easily during image reconstruction.

As an initial proof-of-concept experiment focusing on super-resolution performance, the imaging speed of the LPSIM technique was not pushed to its maximum in this paper.

Based on already-demonstrated 11 Hz SIM imaging [KCG+09], combined with a resonant LP field enhancement factor in the object plane which we have both predicted and observed to be more than 5x, we are confident that future work will demonstrate fast, video-rate imaging capability.

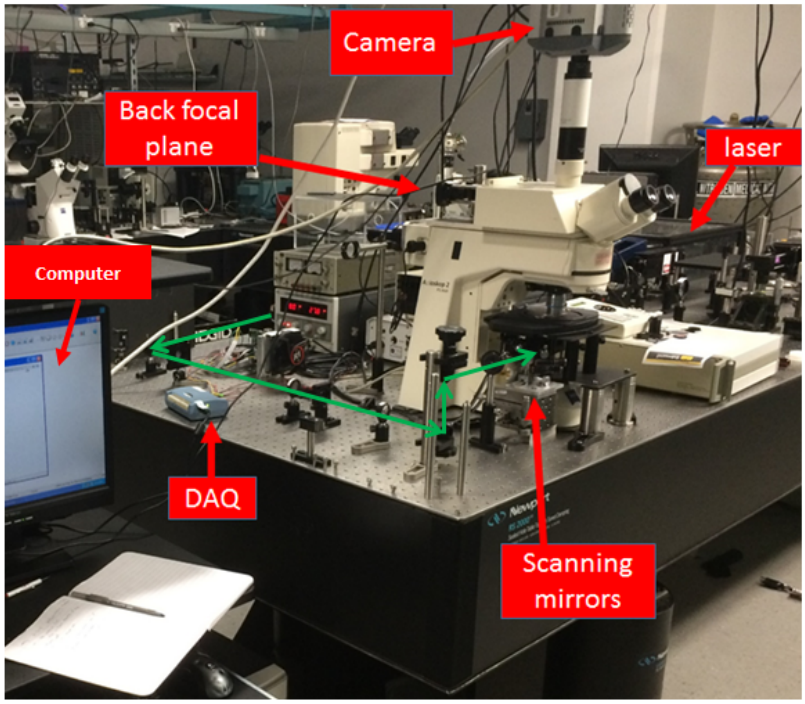

Figure 3.5: LPSIM setup photograph: The LPSIM setup in its uncovered state. Three lasers were aligned along the same axis to easily switch excitation wavelengths for different applications. A back focal plane camera was used for verification of the laser incident angle. During experiment, the optical path was covered the and room was dark.

Fig. 3.5 shows a photograph of the experimental setup. A Measurement Computing 1208HS digital acquisition (DAQ) device was used with a MATLAB script (included in Appendix B) to automate the LPSIM experiment. A preset sequence of nine voltages was sent to each of the mirrors to control incident angle, while a synchronized trigger signal initiated the camera exposures. The captured image data was loaded into MATLAB for super-resolution reconstruction. Fig. 3.6 shows a schematic of the control connections

between various electronics hardware used in the experiment. The mirror module gave output information allowing us to monitor the real mirror angle at high speeds, to ensure that the system was stabilized for each image capture.

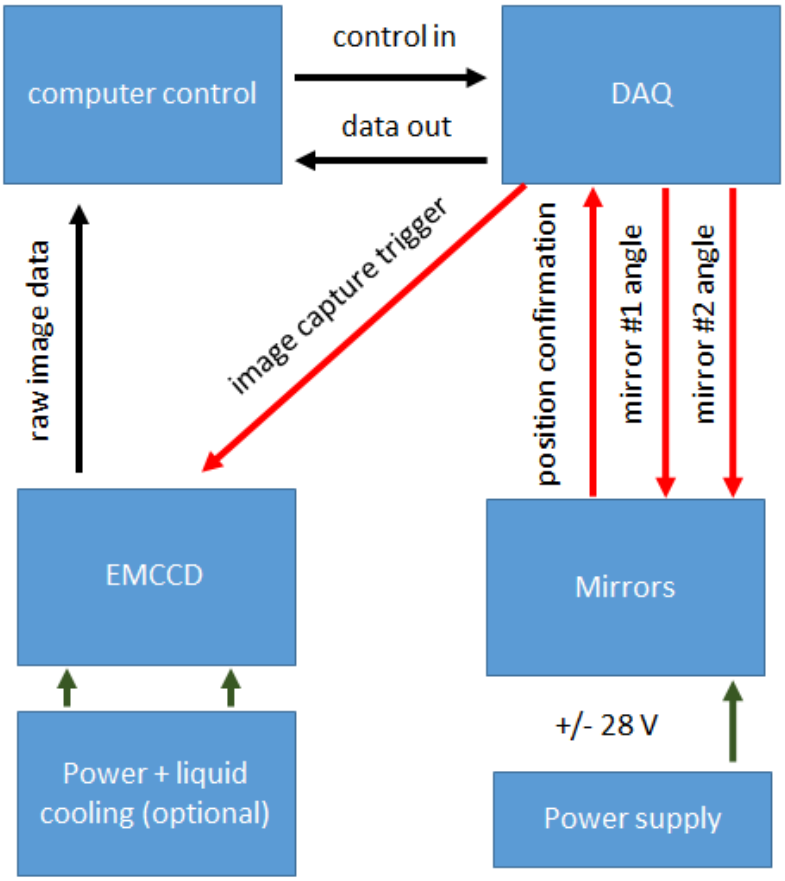

Figure 3.6: Hardware control connections: A computer generates the desired voltage sequence and starts the DAQ. The CCD can be cooled to -80° C with thermoelectric cooling, or to -100° C by circulating chilled water, to reduce electronic noise.

A cylindrical lens in the front of our 4f system corrected for a practical path-length issue. Our two scanning mirrors were separated 5 mm apart along the optical path. Thus, only one could be at the optimal position for our 4f system. The cylindrical lens left the correctly-placed mirror angle unaltered, but adjusted the effective angle of the out-of-position

mirror to give the desired 2D angle sequences.

3.2 Nano-antenna array fabrication

Since the LP fields are determined by local geometry, care was taken in the design and fabrication of our nano-antenna array. The design shown in this work, illustrated in Fig. 3.7(a), is just one of many potential LPSIM geometries that can be used to achieve super resolution of varying degrees. In addition to the geometric parameters, the material properties at the operating frequency are also important. Our final structure was validated via full-wave simulations prior to fabrication. Several factors contribute to the overall design, as several criteria must be met for an effective LPSIM substrate. First, the operating wavelength was chosen to be in the visible range for our application. From there, silver was chosen for its strong plasmonic response. The geometrical parameters of the structures were chosen so that patterns appropriate for LPSIM could be reliably generated.

To get the super-resolution image information, a total of nine diffraction-limited sub-images were collected for each LPSIM image frame. Taking advantage of the three-fold symmetry of our array, the angle was varied three times in each of three planes of incidence, always with in-plane polarization. The fluorescent samples were placed directly on the plasmonic substrate, so that the evanescently-bound LP fields would have a strong effect. Once the sub-images were collected, a straightforward reconstruction algorithm [MBG$^+$12] allowed for an accurate recovery of the super-resolution image, even when the plasmonic excitation patterns were not precisely known.

Shown in Fig. 3.7(c),(d) are SEM images of the real LPSIM geometry from above, and from a cross-section view, at different stages of the fabrication process. Good uniformity is observed over a wide area, which is essential to final image quality. This uniformity is

also shown at a larger scale by the camera image in Fig. 3.7(b).

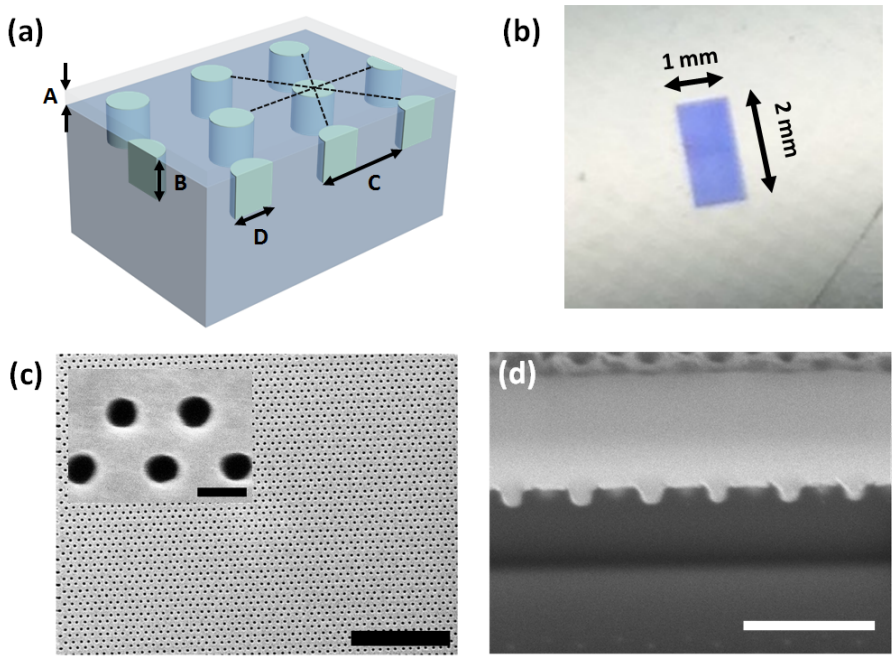

Figure 3.7: Fabrication overview: (a) 3D schematic of a fabricated LPSIM structure. A = 20 nm is the protective layer thickness. B = 60 nm is the disc height. C = 150 nm is the disc pitch. D = 60 nm is the disc radius. (b) Backlit camera image of full patterned area, showing uniform blue/violet LP transmission of silver discs across imaging surface (c) Main: SEM image of nanodisc array mold from above, showing the hexagonal lattice geometry. Scale bar: 2 μm. Left inset: the same mold at a higher magnification. Scale bar: 100 nm. Right inset: SEM image cross-section of an unfinished array prior to silver deposition, with the scale bar representing 300 nm. The etched depth for the nano-antennas is 60 nm.

A protective layer of SiO_2 was sputtered on top of the silver antenna array. This layer serves multiple purposes, and the chosen thickness of 20 nm is carefully optimized. It protects the silver from oxidation and handling damage, it prevents fluorescence quenching, and it protects biological samples from direct contact with silver, with only minimal separation of the object from the evanescent LP field excitation.

We devised a fabrication process using nanoimprinting to allow for repeated, reliable production of many LPSIM substrates without excessive time or cost. Figures 3.8, 3.9, and

3.10 give a detailed summary of the full fabrication process. Nanoimprinting was used to allow for inexpensive, repeatable results. Our three-step etching process was calibrated by cross-sectional scanning electron microscope (SEM) images, as in Fig. 3.7(d), which allowed for accurate adjustment of our etch times.

The nano-antenna geometry was designed via full-wave simulation to provide a 3X resolution enhancement using LPSIM. This scheme is scalable to different wavelengths, as long as a good plasmonic material is available. For this reason, two versions of the LPSIM substrate were made, at different scales. Each patterned covered a 2 mm^2 area, to allow for a very wide super-resolved field of view. Both arrays consisted of a hexagonal lattice of nanodiscs embedded in fused silica.

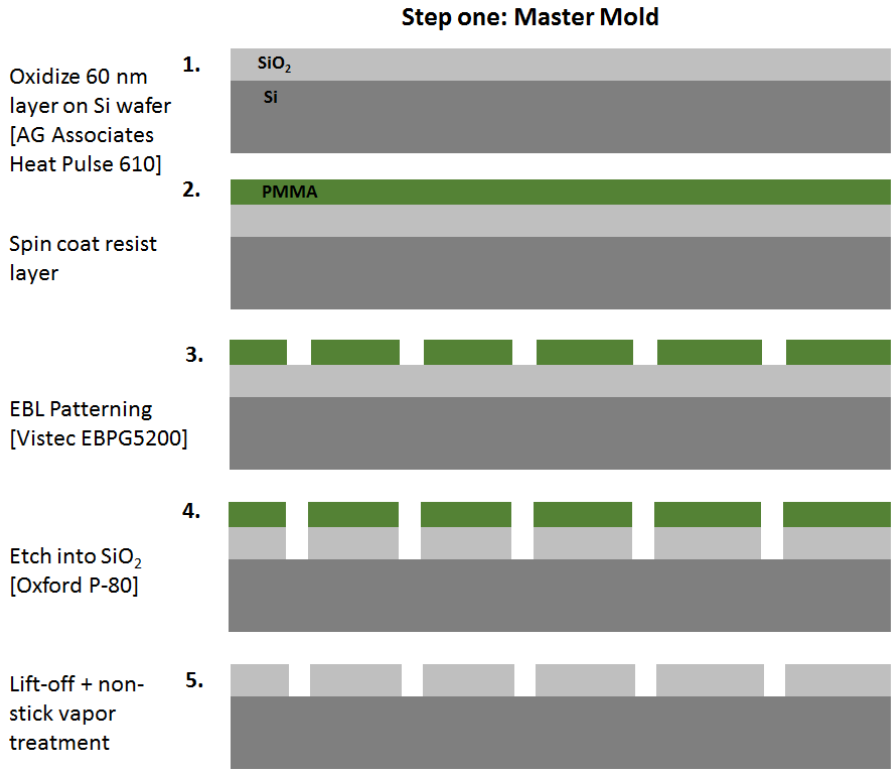

Figure 3.8: Master mold fabrication: This process only had to be done once to make many LPSIM samples.

In the smaller-scaled array, the discs were 60 nm in diameter, 60 nm in height, and

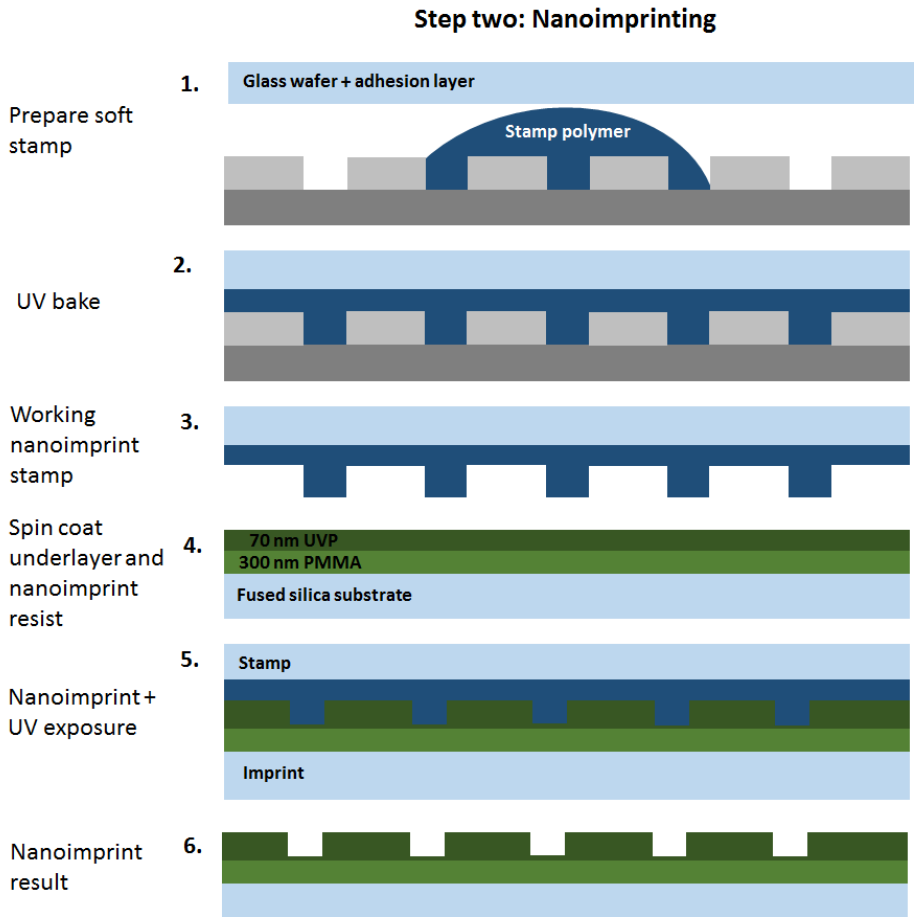

Figure 3.9: Nanoimprinting process: Stamps were made from the master mold. Each stamp could be used for approximately 20 nanoimprints before a new one became necessary.

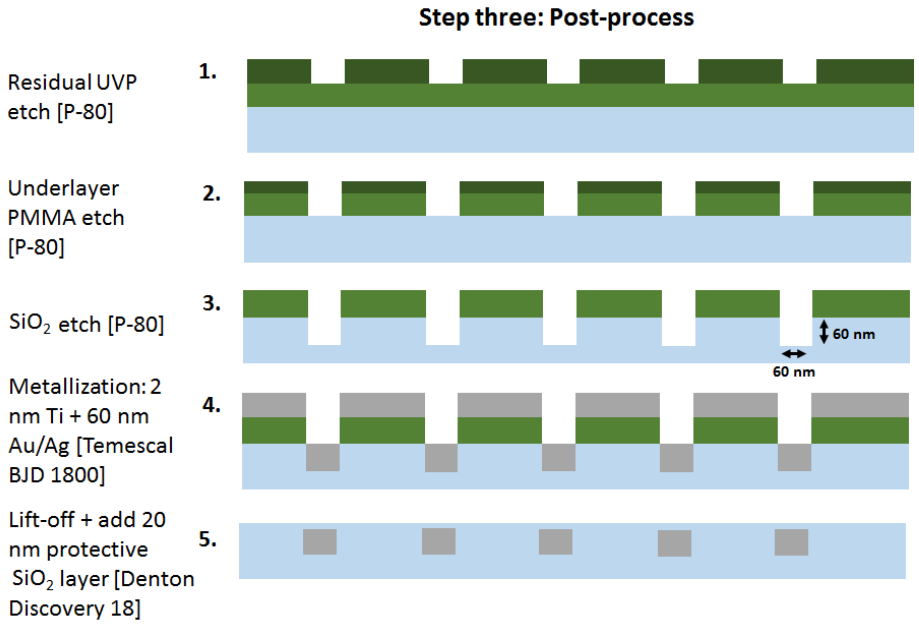

Figure 3.10: Final fabrication steps

spaced 150 nm apart from the nearest neighbor, measured center-to-center. This smaller array was designed to use silver as the metallic element, and works best with laser wavelengths in the short end of the visible spectrum, such as 405 nm or 488 nm. All of our experimental images shown in this work were taken using the smaller-featured array. The larger-featured pattern (shown in Fig. 3.11) had 80 nm diameter discs, still 60 nm in height, spaced 200 nm from their nearest neighbors. This array was designed to use gold as the metallic element, and works best with laser wavelengths in the middle or longer end of the visible spectrum, such as 532 nm. This design can be useful if a particular biological sample is very sensitive to shorter-wavelength light, although the resolution performance will be somewhat less.

One significant advantage of generating structured excitation via local geometry is that the pattern will be less prone to distortion. Whereas in SIM or PSIM, an interference-based standing wave depends on a reliable and undisturbed phase relationship between counter-propagating waves in the object plane, LPSIM does not. If there is a local defect in

the substrate, or if the object itself perturbs the intended field pattern, the defect will not cause the pattern to deteriorate outside of the localized area.

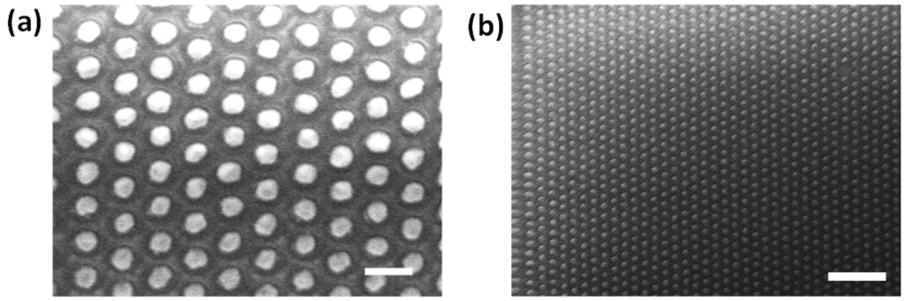

Figure 3.11: SEM images of nano-antenna array: (a),(b) SEM images of nanodisc array from above, showing silver discs arranged in a hexagonal lattice. Shown here is the larger-featured array, with disc diameter of 80 nm and pitch of 200 nm. Scale bars represent 200 nm and 1 μm, respectively.

The fabrication of our LPSIM substrates was centered on a nanoimprinting process to ensure cost-effective, timely repeatability. All fabrication steps took place in the Nano3 cleanroom facility at University of California, San Diego. The master mold was formed on a silicon wafer. A 60 nm layer was oxidized, and then spin coated with poly(methyl methacrylate) (PMMA). Electron beam lithography (EBL) patterning of the hexagonal array geometry was done with a Vistec EBPG5200. The pattern was etched into the oxidized layer. All etching steps in this fabrication process were done with an Oxford Plasmalab 80. After lift-off of the resist layer, the master mold was coated with a non-stick vapor treatment. The stamp polymer, shaped by the master mold, was adhered to a glass wafer in an ultraviolet oven to create the soft nanoimprint stamp. The LPSIM substrate began with a fused silica wafer, coated with a 300 nm PMMA resist under-layer, and then a 70 nm top-layer of UV resist (I-UVP, EZ Imprinting). This bilayer resist was stamped using an EVG620 mask alignment system. The nanoimprinted pattern was etched into the fused silica LPSIM substrate. Metal deposition was done with a Temescal BJD 1800 electron

beam evaporator, and included a 2 nm titanium adhesion layer. After lift-off of the resist and unwanted metal, a 20 nm spacer layer of SiO2 was deposited with a Denton Discovery 18 sputtering system.

The etching conditions in the chamber of a shared etching machine are not always consistent, so scratch tests on a dummy sample were used to calibrate the true etch depth for each fabrication run. The calibration scratch profile was measured with a Dektak 150 surface profiler. However, since the real substrate etch involves etching into high aspect ratio holes, the dummy sample is not always a strictly reliable indicator. For this reason, additional validation of the finished sample with an atomic force microscope (AFM) was done to confirm that the etched depth and deposited silver height were close to the desired parameters. An example AFM image of a less-than-perfect result is shown in Fig. 3.12.

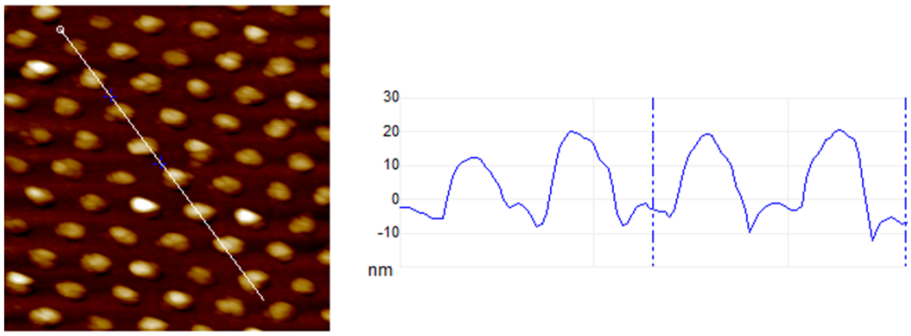

Figure 3.12: AFM validation of fabrication result: An AFM image (left) and profile (right) along the white line in the image shows 10 to 20 nm height variation across the sample. In this case, the imperfect flatness of the surface is a result of slower etching conditions into a high aspect ratio hole geometry. Because the holes were etched slightly less than intended, the silver protrudes somewhat from the surface. However, small unevenness as shown here is usually acceptable for imaging with a blind reconstruction method. For lateral scale, note that the pitch of the nano-antenna array is 150 nm.

Another verification step is measurement of the dark field scattering spectrum. To a

rough approximation, the LPs present in the LPSIM substrate are intuitively comparable to the dipole resonance of a sphere, which can be solved analytically [Mai07]. However, there are many differences found in the LPSIM antenna array. First, the cylinder geometry is more complex and lends itself to modes at the corner of the cylinder. Second, the dipole behavior is redshifted to longer wavelengths due to the high index of the SiO_2 surrounding media. Third, and importantly, there is an additional redshift provided by near-field coupling in the array. The dipole resonance can be thought of as a spring, with a displacement of charge from an external electric field, and a restoring force due to Coulomb repulsion. The spring constant κ is related to the spring's resonant frequency $\omega_0 \sim \sqrt{\kappa}$. The longitudinal dipole modes of each antenna will lower the restoring force for the neighboring antennas, thus shifting the resonance to longer wavelengths. Observed violet transmission in Fig. 3.7 is a result of the relatively weak scattering at that wavelength, when illuminating with a white backlight. The strong, clean scattering peak indicates a consistent nano-antenna geometry, and a good fabrication result.

During development of the fabrication process, several challenges were encountered and overcome. One challenge of particular interest involved the reactive ion etching step. The PMMA resist underlayer is susceptible to hardening at high temperatures. The etching process, if done in single-shots, subjects the sample to high enough temperatures that the PMMA becomes very difficult to lift off of the SiO_2 substrate. To solve this problem, the etching recipe was adapted to avoid high temperatures by etching in periods of just ten seconds, followed by a cool-down period. This approach entails somewhat longer sessions on the etching machine, but successfully avoids hardening the PMMA.

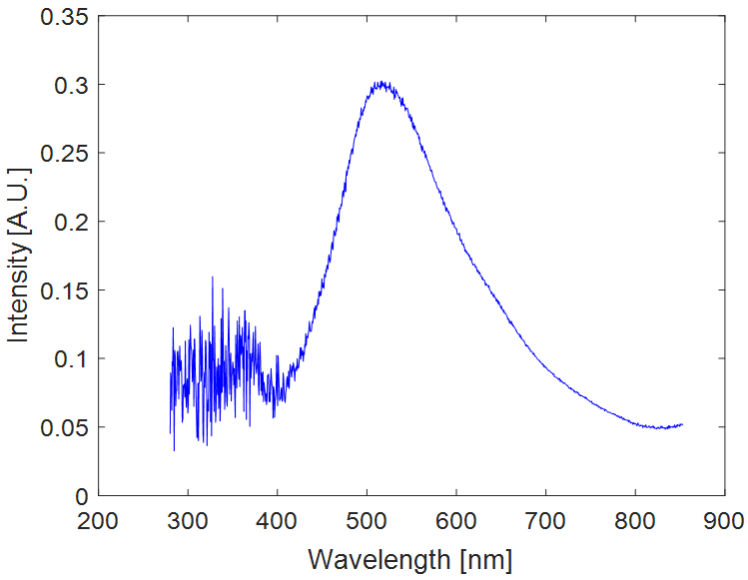

Figure 3.13: Dark field spectrum of LPSIM substrate: Measurement taken with Andor SR-303-B spectrograph and Andor Newton 920 CCD. The sample was illuminated with a halogen lamp. A clear scattering peak is present.

3.3 Experimental super resolution imaging

To test the super-resolution performance of our LPSIM setup, a random distribution of fluorescent polystyrene beads was used as a simple object. The beads had 50 nm diameter, and were excited by a 405 nm laser with an initial output power of 150 mW. The beads (Fluoresbrite YG Microspheres) exhibited filtered fluorescent emission centered around 500 nm. Beads were drop-cast directly onto the LPSIM substrate, fixed, and imaged with an Olympus UPLSAPO 60XW water immersion objective. The fluorescent beads were diluted in water and drop-cast onto the LPSIM substrate. After air-drying, the substrate was rinsed to reduce loose fluorescence.

Characterization of the resolving power was done by looking at both single-bead full-width half-maximum (FWHM) as well as two-bead separation. Fig. 3.14(a),(c),(e) show the imaging results of a single bead, with a LPSIM FWHM of just 74 nm, which is

approximately 1/3 the diffraction-limited FWHM, as expected. Fig. 3.14(b),(d),(f) show two closely-spaced beads, which are unresolvable under normal imaging conditions, but can be clearly resolved via LPSIM. The center-to-center spacing of the beads was 78 nm, which means the edge-to-edge gap between them was approximately 28 nm. Fig. 3.14(g)-(j) show the Fourier space and real space results of a larger distribution of beads, both with and without the LPSIM technique applied. We find confirmation that the OTF is dramatically enlarged by the LPSIM technique, in agreement with the expected 3X improvement. Over a wide area, a clean, super-resolved image is obtained, with minimal distortion.

One motivation for super-resolution imaging is to be found in cellular biology. Genomic and neuronal activities in particular are hot areas of research. As an initial demonstration of bio-compatibility and general imaging capability, we used our LPSIM technique to image neuron cells expressing Fzd3-tdTomato. This particular type of sample is of interest [OSL$^+$13] in understanding how growth cones steer themselves within their environment. Relevant features of Fzd3-containing vesicles can be as small as 50 to 100 nm in diameter. LPSIM is well-suited for use with this type of sample. For the tdTomato emission, the minimum resolvable feature size under the diffraction limit was 240 nm, but using LPSIM we observe resolution down to $\sim$80 nm. As shown in Fig. 5, important sub-cellular features can be imaged at much greater resolution ($\sim$3x) compared with the diffraction-limited case.

To prepare this biological sample, rat E13 embryos of either sex were eviscerated, and the notochord was removed. Using a pulled glass needle, Fzd3-tdTomato expressing plasmids [OSL$^+$13] was injected into the neural tube. Using 5 mm gold-plated electrodes (#45-0115; Harvard Apparatus, South Natick, MA), square-wave current was passed across the dorsal neural tube using a BTX #ECM 830 electroporator. Electroporation conditions

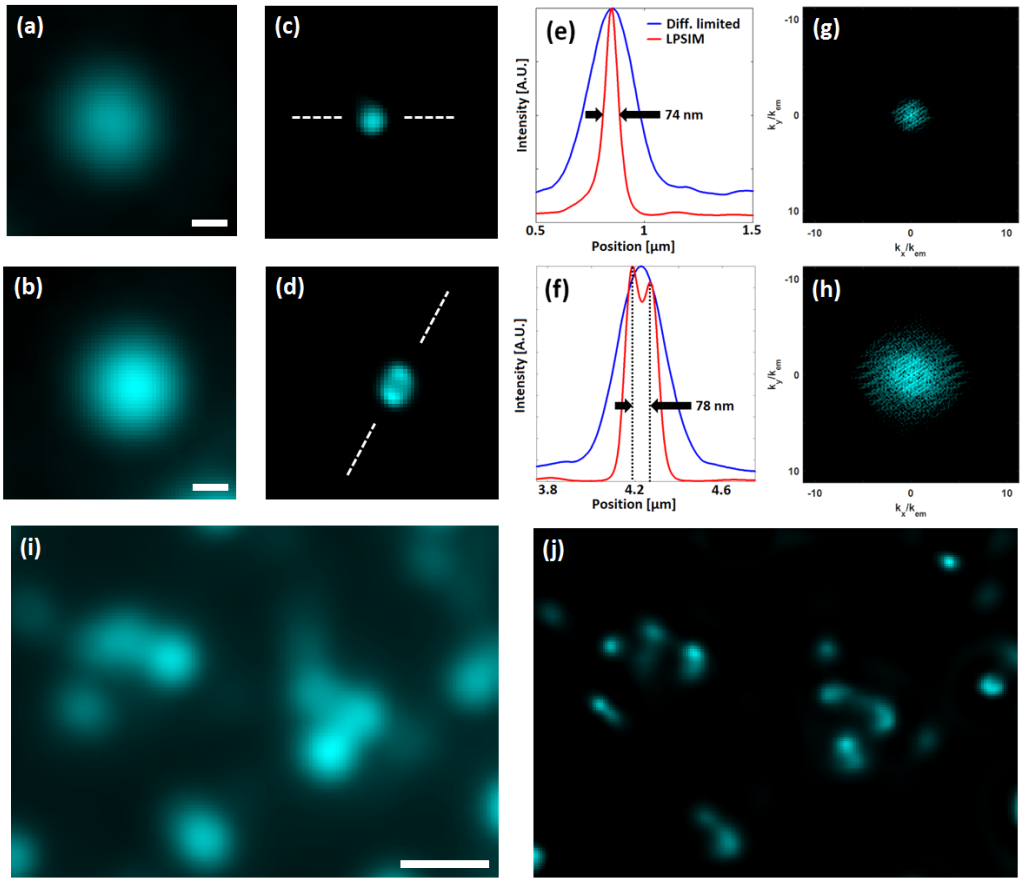

Figure 3.14: Demonstration of super resolution performance: (a) Diffraction-limited image of a 50 nm diameter fluorescent bead. Scale bar: 120 nm. (b) Diffraction-limited image of an unresolved pair of beads. Scale bar: 120 nm. (c) LPSIM image of *(a)* with significantly improved resolution. (d) LPSIM image successfully resolving the closely spaced beads in *(b)*. (e) Normalized intensity profile of the images in *(a)* and *(c)*, along the dashed white line. The FWHM of the bead image in *(c)* is 74 nm. (f) Intensity profile showing resolution of two beads spaced 78 nm apart. (g),(h) Spatial frequency spectra (log-scale amplitude) of a standard and LPSIM image, respectively. The LPSIM technique increases the spatial bandwidth of the imaging process by a factor of approximately three. (i),(j) Diffraction-limited and LPSIM images of many beads within a wider area. Scale bar: 0.5 μm.

were as follows: three pulses, 25 V, 100 ms pulse, 1 s interval. After electroporation, the spinal cord was dissected and dissociated commissural neurons were plated on the matrix coated with 20 μg/ml PDL. After 2 DIV, the neurons were fixed in 4% PFA for 15 min at 37° C and mounted in Fluoromount G. Experiments were conducted in accordance with the NIH Guide for the Care and Use of Laboratory Animals and approved by the UCSD Animal Subjects Committee.

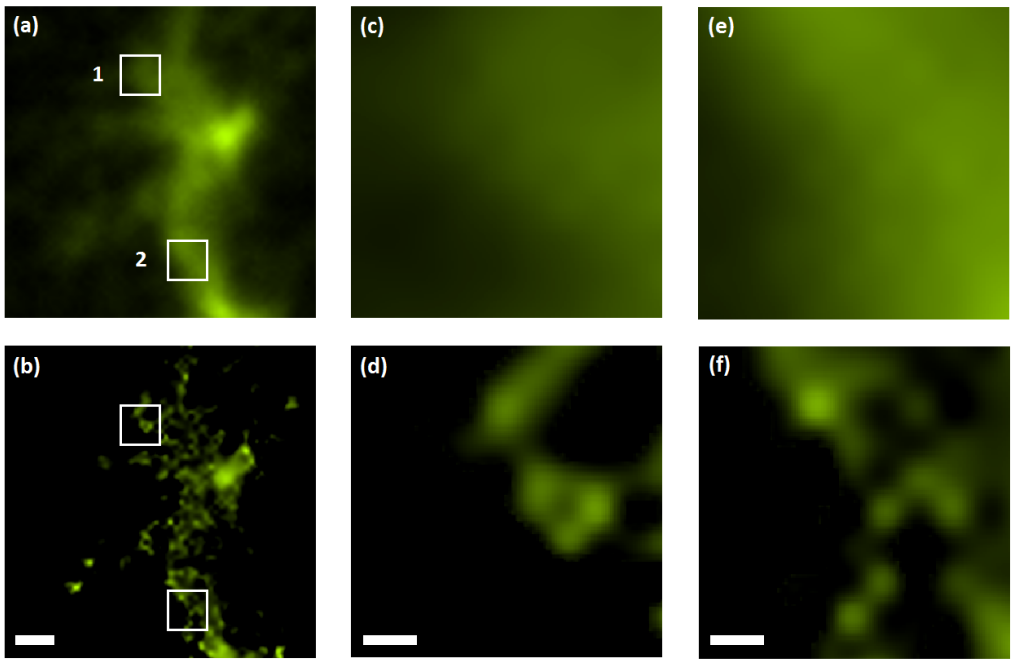

Figure 3.15: LPSIM fluorescence imaging results for a fixed neuron cell: Fzd3 receptors were labeled with tdTomato. A 150 mW, 488 nm laser was used for illumination. The central fluorescence wavelength was 570 nm. (a),(b) Wide-field diffraction-limited and LPSIM images, showing consistent, dramatic resolution enhancement over the full area. Scale bar: 500 nm. (c),(d) A closer look at the area inside box 1 from (a) and (b), showing clear resolution of fine features, consistent with theoretical expectations, which are not detectable in the diffraction-limited image. Scale bar: 100 nm. (e),(f) A closer look at the area inside box 2. Scale bar: 100 nm.

In many practical cases, the LPSIM technique offers an optimal balance between the many factors influencing the usefulness of an image to biologists. LPSIM does not require

point-scanning to generate the image. The nano-antenna fields are scanned in parallel, so the field of view is limited only by optics and the area of the fabricated substrate itself, and can be increased without sacrificing imaging speed. The resonant LP fields decay exponentially away from the substrate. Therefore, the vast majority of the fluorescent signal comes from the surface of the object, as is essential for fluorescent imaging. Additional post-processing can be used [NJW97] to remove any remaining out-of-plane noise. The resonant plasmonic enhancement of the LP fields in our optimized structure provides several advantages. For one, the local enhancement allows for strong excitation of the targeted fluorescent labels without using an unnecessarily high-powered laser, or irradiating the entire sample with strong intensity. The resonant excitation also allows for shorter exposure times and faster imaging speed, since the strongly excited signal will be boosted relative to the noise sources present in a given experiment.

The LPSIM substrate's protective layer dramatically improves durability and compatibility with biological samples. However, SiO_2 is somewhat permeable to oxygen, and so the silver generally degrades after several months due to oxidation. This degradation can be slowed by storing in a vacuum, when possible. If the protective layer seal is imperfect, due to etching inaccuracies or other issues, then certain biological preparation procedures requiring harsh chemicals may cause destruction of the silver structure. When possible, this risk can be avoided by doing the initial preparation of the biological sample on a cover slip rather than on the substrate itself.

The super-resolution performance achieved in this work was consistent and robust for the various samples tested. The resolution could easily be incrementally improved by using shorter laser wavelengths or a higher-NA objective, in combination with an appropriately designed LPSIM substrate. Due to the dependence of LP resonances on particle size

[KCZS03], and the various emission spectra of available fluorescent dyes, this technique is readily scalable to different operating wavelengths. To push resolution even further, more complex substrate designs possibly incorporating both LP and SPP structure into the excitation patterns may hold promise. The technique shown here should prove useful for a multitude of fluorescence imaging applications, especially for biological surface dynamics.

3.4 The blind reconstruction algorithm

Because the LP field excitation patterns in the LPSIM method were generated on nano-antennas rather than via a standing wave, the structured illumination profile was not a simple shifted sine wave, as is the case for many SIM experiments. Although the LPSIM substrate was carefully designed and simulated to ensure it would provide the appropriate patterns for super-resolution, it is difficult to expect perfect knowledge of the real patterns at the 60 nm scale, due to fabrication tolerances and other sources of experimental error. To reconstruct a super-resolution image using the more complex, quasi-periodic patterns and pattern shifts present in LPSIM, a variant of blind-SIM [MBG$^+$12] was implemented with a MATLAB algorithm, as shown in Appendix A. This reconstruction method is very useful as it does not require perfect knowledge of the real excitation patterns. Suppose an unknown fluorescent-tagged object o is excited by nine LP field patterns $I_{(l=1,\ldots,9)}$. For each pattern, the image m recorded by the camera is the convolution of the excited object and the PSF,

$$m_l(\mathbf{r} \in \Gamma) = \int_{\Omega} o(\mathbf{r}')I_l(\mathbf{r}')p(\mathbf{r}-\mathbf{r}')\mathrm{d}\mathbf{r}' \tag{3.1}$$

where $\mathbf{r}$ is the position in the object plane, and p is the PSF. Γ represents the measurement plane, and Ω represents the object plane. We can abbreviate the expression for

m by defining an operator $\mathbf{A}$,

$$m_l = \mathbf{A}(I_l o) \tag{3.2}$$

and we can specify the residual error R between the expected and measured image,

$$R_l = m_l - \mathbf{A}(I_l o) \tag{3.3}$$

Remember that all matrix "multiplication" here is actually the element-by-element Hadamard product. In this "blind" scheme, both the object o and the excitation patterns I_l are treated as unknowns. So, we have 9 equations and ten unknowns. To make this system of equations solvable, an additional constraint must be introduced.

If it is assumed that over the nine sub-images, the total excitation is approximately equal throughout the object plane, then we can write

$$I_9 = 9\bar{I} - \sum_{l=1}^{8} I_l \tag{3.4}$$

where $\bar{I}$ is the average excitation intensity. An iterative error-minimization algorithm is used to steadily improve initial estimates for the 9 unknown 2D matrices: o, and $I_{(1,\ldots,8)}$.

Thus we can define a cost function

$$\mathcal{F}(o, \{I_l\}) = \sum_{l=1}^{9} \|R_l\|^2 = \sum_{l=1}^{8} \|m_l - (I_l o) * p\|^2 + \|m_9 - (I_9 o) * p\|^2 \tag{3.5}$$

where $*$ represents convolution. Iteratively improved estimates for o_n and $I_{(l,n)}$ (where n represents the iteration count) are found using the conjugate gradient method. A

sequence of updated guesses are built for the object and illumination patterns,

$$o_n = o_{n-1} + \alpha_n d_{o,n}$$
$$I_{l,n} = I_{l,n-1} + \beta_{l,n} d_{I_l,n} \tag{3.6}$$

where α and β represent step size coefficients, and d is the updating direction. This direction is calculated based on the gradients of the cost functional with respect to each unknown matrix. The directional derivative $D(u)$ with respect to the object matrix is

$$D^o(u) = \lim_{s\to 0} \frac{\mathcal{F}(I_l, o+su) - \mathcal{F}(I_l, o)}{s} \tag{3.7}$$

where s is a constant step size. This expression can be re-written,

$$\begin{aligned} D^o(u) &= \lim_{s\to 0} \frac{\sum_{l=1}^{9} \|m_l - \mathbf{A}(I_l o) - \mathbf{A}(I_l su)\|_\Gamma^2 - \|m_l - \mathbf{A}(I_l o)\|_\Gamma^2}{s} \\ &= \lim_{s\to 0} \frac{-2\sum_{l=1}^{9} \langle m_l - \mathbf{A}(I_l o) | \mathbf{A}(I_l su)\rangle_\Gamma + \|\mathbf{A}(I_l su)\|_\Gamma^2}{s} \\ &= -2\sum_{l=1}^{9} \langle R_l | \mathbf{A}(I_l u)\rangle_\Gamma \\ &= -2\sum_{l=1}^{9} \langle I_l \mathbf{A}^\dagger R_l | u\rangle_\Omega \end{aligned} \tag{3.8}$$

Where $\langle\cdot|\cdot\rangle$ represents the inner product and † denotes the Hermitian adjoint. The

gradient is the function that maximizes D,

$$g_o = -\sum_{l=1}^{9} I_l \mathbf{A}^{\dagger} R_l \tag{3.9}$$

In a similar manner, the gradient for each illumination pattern can also be calculated,

$$D^{I_l}(u) = \lim_{s\to 0} \frac{\mathcal{F}(I_l + su, o) - \mathcal{F}(I_l, o)}{s}$$

$$= -2\langle R_l | \mathbf{A}(ou)\rangle_{\Gamma} + 2\langle R_L | \mathbf{A}(ou)\rangle_{\Gamma} \tag{3.10}$$

$$= -2\langle o\mathbf{A}^{\dagger}(R_l - R_L) | u\rangle_{\Omega}$$

$$g_{I_l} = -o\mathbf{A}^{\dagger}(R_l - R_L) \tag{3.11}$$

Using the conjugate gradient method, we define our updating directions at each iterative step as

$$d_{o,n} = g_{o,n} + \gamma_{o,n} d_{o,n-1}$$

$$d_{I_l,n} = g_{I_l,n} + \gamma_{I_l,n} d_{I_l,n-1} \tag{3.12}$$

where γ is defined as

$$\gamma_n = \frac{\langle g_n | g_n - g_{n-1} \rangle_\Omega}{\| g_{n-1} \|_\Omega^2} \tag{3.13}$$

Since the real object intensity can never be negative, a positivity constraint was incorporated into the cost function, improving reconstruction stability with respect to experimental noise. It can also be shown that the operator **A** is equal to its own Hermitian adjoint for a real-valued, symmetrical PSF, which simplifies our reconstruction algorithm. Fig. 3.16 shows the reconstruction convergence for an example set of data. After 80 iterations, the cost function has been reduced by approximately two orders of magnitude.

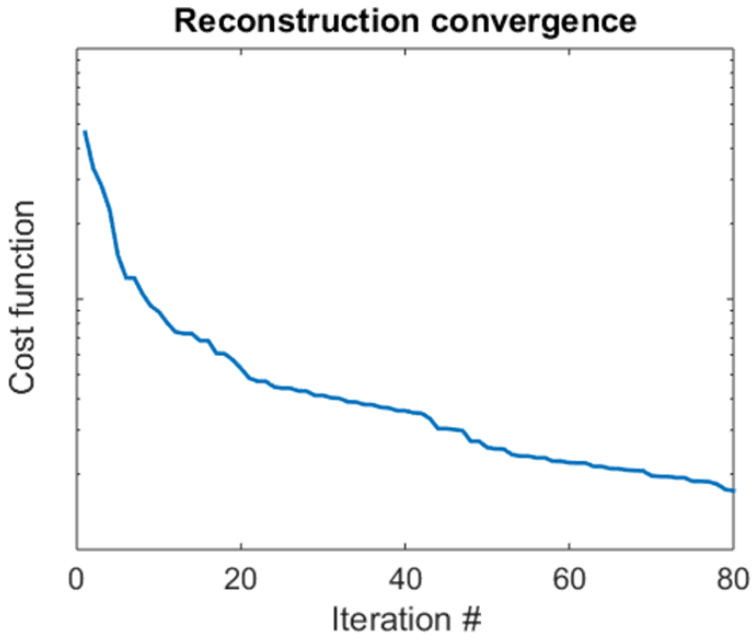

Figure 3.16: Reconstruction convergence: Plot of the cost function reduction (in log scale) with respect to iteration number. For most LPSIM images, 60 to 100 iterations is sufficient to converge to a super-resolution image. After this point, changes to the image are usually minor.

The camera pixels, with magnification, had 67 nm effective size. To improve the smoothness of the final reconstruction, the measured images were interpolated prior to

reconstruction. Occasional experimental drift was also corrected using reference point orientation for each sub-image, when necessary.

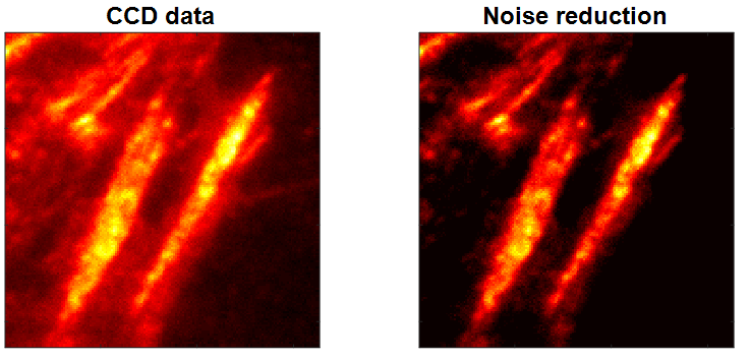

Figure 3.17: Sub-image preprocessing: Left, raw image data from the CCD, from an example biological specimen. Right, the result of preprocessing for the (still diffraction-limited) sub-image. The objects of interest are undisturbed, but the SNR is enhanced.

Especially for biological samples, the raw captured fluorescent image was often noisy, due to loose fluorescence and out-of-plane signal from a thick object. To help the reconstruction proceed more smoothly, automated de-noising was added as a preprocessing step. First, a simple Gaussian smoothing filter was applied to mitigate any single-pixel electronic noise. Then, objects in the field of view above a threshold intensity were emphasized relative to low spatial frequency background noise. An example result can be seen in Fig. 3.17. For certain convenient objects such as fluorescent microspheres, this preprocessing was less important.

Chapter 3, in part, is a reprint of the material as submitted to Nature Photonics, 2016. Joseph L. Ponsetto, Anna S. Bezryadina, Feifei Wei, Keisuke Onishi, Hao Shen, Eric Huang, Lorenzo Ferrari, Qian Ma, Yimin Zou, Zhaowei Liu, “Experimental demonstration of wide-field super resolution surface imaging with localized plasmonic structured illumination

microscopy". The dissertation author was the first author of this paper.

Chapter 4

Numerical study of 3D hyperlens imaging

The development of nanostructured metamaterials and the ability to engineer material dispersion has led to impressive advances in the diverse field of nanophotonics. Of interest to many is the enhanced ability to control, illuminate, and image with light on subwavelength scales. In this chapter, we numerically demonstrate a hyperlens with unprecedented radial-resolution at 5 nm scale for both imaging and lithography applications. Both processes are shown to have accuracy that surpasses the Abbe diffraction limit in the radial direction, which has potential applications for 3D imaging and lithography. Design optimization is discussed with regards to several important hyperlens parameters.

4.1 Physical principles of the hyperlens

The optical microscope has been enabling important scientific discoveries since its invention centuries ago. The ability to observe features and processes otherwise invisible

to the human eye has broadened the scope of scientific knowledge considerably, especially in life sciences and microelectronics. The resolution of a standard microscope is limited, however, by the Abbe diffraction limit [BW99] to approximately 200 nm for visible light wavelengths. To observe elusive sub-diffraction features, various approaches are used such as near-field scanning optical microscopy (NSOM) [HSW$^+$00], stochastic optical reconstruction microscopy (STORM) [RBZ06], photoactivated localization microscopy (PALM) [BPS$^+$06] and saturated structured illumination microscopy (SSIM) [Gus05]. However, most of these methods involve high-intensity light or slow scanning processes, which limits usefulness for imaging sensitive, dynamic biological samples.

With the realization and exploitation of negative index materials [Ves68], many new imaging tools have been developed at optical frequencies. The perfect lens [Pen00] was proposed to aid in high-resolution imaging by allowing detection of larger wavevectors, which ordinarily are lost to evanescent decay. In recent years, many variations of the perfect lens idea have been proposed and demonstrated, including the cylindrical perfect lens [Pen03], and the superlens [FLSZ05], but these all rely on near-field imaging techniques.

As fabrication abilities have improved, thin metal-dielectric multilayer structures possessing hyperbolic dispersion relations have emerged as a way to capture evanescent details in the far-field. These structures, when used for imaging, are known as hyperlenses [SE06][JAN06][LLX$^+$07b][LLX$^+$07a]. A hyperlens is comprised of alternating metal and dielectric planar layers with deeply sub-wavelength thicknesses.

Because of the aforementioned dispersion relation, large wavevectors that decay exponentially in free space may propagate along the radial (ρ) direction in a hyperlens. Additionally, by curving the overall multilayer into a concentric structure, a magnifying effect is obtained, which gradually shrinks the spatial frequency components as they reach layers

with larger radii. By careful design, this can transform high-spatial-frequency information into the collectable aperture of an otherwise standard optical system. This is the primary function of the hyperlens as an imaging apparatus.

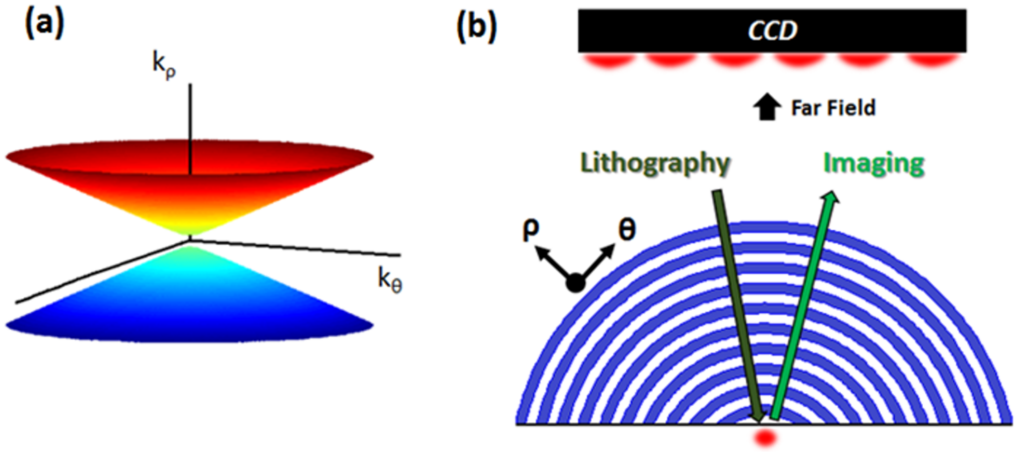

Figure 4.1: Hyperlens conceptual overview: (a) Isofrequency surface in a hyperbolic metamaterial with $\varepsilon_\rho < 0$ and $\varepsilon_\theta > 0$. (b) Illustration of a hyperlens structure, showing the time reversal concept. If a point source imaged by a hyperlens produces a given wavefront at the CCD plane, then the same distribution (accounting for losses) sent in the opposite direction will focus to a point on the other side of the hyperlens.

The concept of time reversal in electromagnetics [LdRTF07][BLZ09] allows us to think of the hyperlens as having two potential applications for both imaging and lithography [XLZ09], as illustrated schematically in Fig. 4.1(b). In one direction, high spatial frequencies from a source are converted to propagating light and collected at a detector such as a charge-coupled device (CCD). This is the imaging configuration. In the opposite direction, a specially-designed diffraction-limited wavefront can be sent into the hyperlens and have its features spatially compressed, resulting in a sub-wavelength focus point for use in lithography.

In past work on hyperlenses, super resolution has been primarily discussed only in the lateral direction. Pyramid-shaped hyperlenses have been designed [CW09] with a specialized

geometry that enables some limited sub-diffraction imaging of sources distributed in three dimensions. However, with this method, there is no clear way to discern the z-position of an object without a priori knowledge. In our paper, we look carefully at the radial resolution of a spherical multilayer hyperlens. The dispersion and geometry of this design allows for far-field focusing behavior that is highly sensitive to radial position. We show the ability to resolve differences in radial position as small as 5 nm, in concert with lateral super resolution, via simple far-field detection.

Any significant z separation between an object and the hyperlens surface has, to date, been regarded as sub-optimal, since the evanescent field strength drops off exponentially away from the object. However, within a thin volume close to the surface, evanescent fields from objects with a distribution of z depths can be focused and imaged in the far-field. This allows for three dimensional super resolution imaging and lithography.

4.2 Numerical 3D imaging results

To examine the imaging capability of a hyperlens in the radial direction, two-dimensional full-wave simulations using COMSOL Multiphysics were conducted. The polarization-dependent behavior of the hyperlens dictates that only the transverse magnetic (TM) field components will propagate and contribute to a resolved image. Transverse electric (TE) components will be reflected and will neither contribute to nor degrade the hyperlens performance [RYX$^+$10]. A TM-polarized point source was placed several nanometers away from the hyperlens surface, and the propagation through the hyperlens and out on the other side was monitored. For the most realistic result, a real multilayer structure was used in our model. The metal layer material used was silver (ε_m = -2.4 - 0.25i). The dielectric layers had permittivity ε_d = 3.75, and the imaging half space had a permittivity of 3.217.

The real permittivity in the vicinity of the point sources was chosen as 2.89. The real silver permittivity for 365 nm light was based on an interpolation of previous experimental measurements [JC72]. The metal filling fraction p was 0.5. For these calculations, the radii of the inner and outer hyperlens layers were 400 nm and 1840 nm, respectively. Numerical calculation time was shortened by restricting the simulated region to a central area where the vast majority of the field strength was concentrated. This restriction is acceptable because the anisotropic nature of the hyperlens medium prevents significant propagation in the tangential direction. Perfectly matched layer boundaries were added at the top and bottom of the simulation region to reduce unwanted reflections. Results are shown in Fig. 4.2.

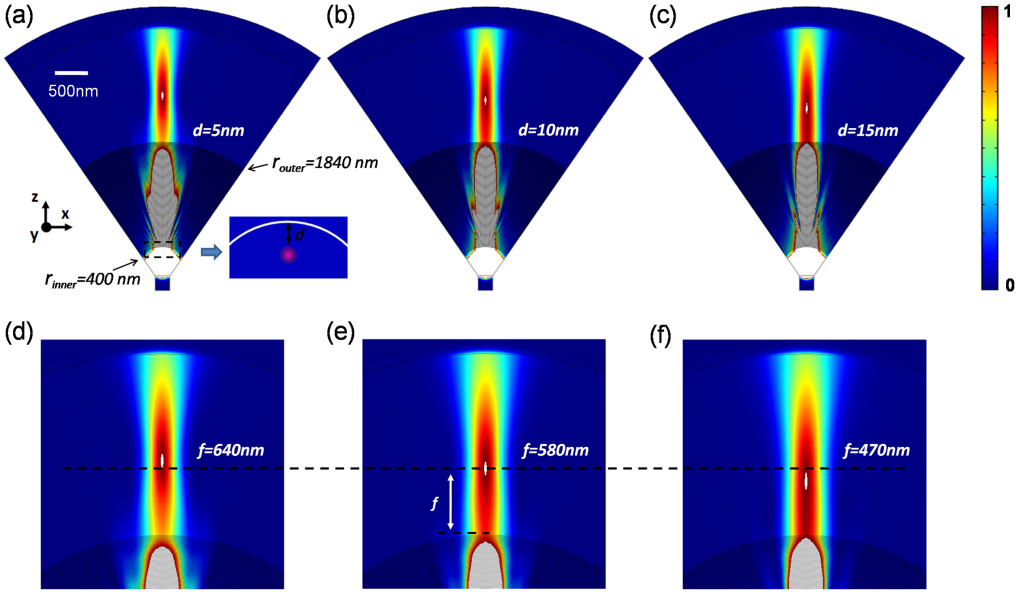

Figure 4.2: Hyperlens imaging depth resolution: (a)-(c) Intensity distributions for imaging of a point source at varying separations d (5, 10, 15 nm) from the inner hyperlens surface. The radii of the inner and outer hyperlens layers were 400 nm and 1840 nm, respectively. The thickness of each layer is 10 nm. The colorbar represents the normalized, linear-scale intensity. Note that the white areas indicate "saturated" intensity above the normalization value, which was chosen for illustrative purposes to show the focus spot clearly. (d)-(f) A closer look at the intensity focus spot movement in *(a)-(c)*. The focal positions away from the outermost surface (f) are 640, 580, 470 nm, respectively. The white scale bar in *(a)* represents 500 nm.

The radial separation of the point source from the hyperlens surface was set to d = 5, 10 and 15 nm. In all cases, the emitted light captured by the hyperlens was refocused to a point f (defined along the radial direction) away from the outermost surface of the hyperlens, which was defined as $f = 0$. Note that the results for each of the three separations were contrasted to clearly show the focus point. For separations of 5, 10 and 15 nm, the focus position was at f = 640, 580 and 470 nm, respectively. We see that the focus point position f varies significantly when d is changed.

As light travels through the hyperlens, the lateral k-vectors from the object are compressed and the resulting image is projected into the far-field. The change in f with respect to the change in d is also magnified, nearly by a factor of 17. This has potential to bring very fine depth resolution into a far-field measurement. In Fig. 4.2(b), we see a close look at the focus spot movement as a function of d. For only a ten nanometer change in d, we have more than 150 nm change in f, which can be detected quite easily using mechanical translation stages.

Figure 4.3(a) shows the simultaneous focusing result for two point sources. As pictured in Fig. 4.3(b), although the sources are 130 nm apart in x, and just 10 nm apart in ρ, their far-field focus points are dramatically separated on the other side of the hyperlens (160 nm apart in ρ and even further separated in x). Because the light is steered along in the ρ direction within the hyperlens, the small initial separation is magnified considerably.

The hyperlens is well known to have sub-diffraction imaging capability in the lateral direction. We have shown here that in addition, extremely fine radial resolution can be achieved. This is a coveted capability for imaging of biological specimens. By stepping a motorized z-stage, or potentially by recording in multiple z-planes simultaneously, a three-dimensional image can be obtained, although the total image depth in z direction is

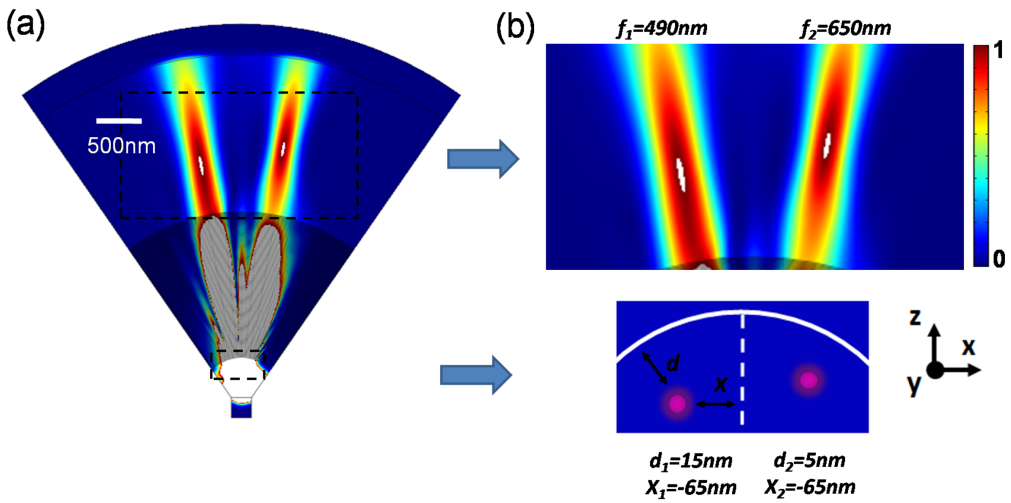

Figure 4.3: Hyperlens imaging two point resolution: (a) Imaging result for two 365 nm sources, showing focusing at two different positions for the two sources. The white scale bar represents 500 nm. (b) Magnified view of the focus spots and a schematic illustration of the source positions. The two point sources are 130 nm apart in x, and just 10 nm apart in the radial (ρ) direction. The far-field foci differ by 160 nm in ρ.

always limited by the evanescent wave decay length.

4.3 Hyperlens design parameters

Many geometrical variations of the multilayer hyperlens [XLZ09][MZC+11] have been explored for the overall shape of the multilayer structure, ranging from flat to spherical to trumpet shapes. For shaping and focusing wavefronts in the manner of a lens, a broad spatial curvature is favored.

Analysis based on effective medium theory (EMT) [LLX+07a] of a subwavelength, anisotropic multilayer structure such as a hyperlens reveals a hyperbolic dispersion relation, as shown in Fig. 4.1(a) and described as,

$$\frac{k_\theta^2}{\varepsilon_\rho^2} + \frac{k_\rho^2}{\varepsilon_\theta^2} = \frac{\omega^2}{c^2} \tag{4.1}$$

where k_θ and k_ρ represent the wavevector components in orthogonal directions, ω is the angular frequency, and c is the speed of light. ε_ρ is the permittivity in the ρ direction, while ε_θ is the permittivity in the θ plane, which is parallel to the layer orientation as shown in Fig. 4.1(b). The permittivities are defined as

$$\varepsilon_\theta = p\varepsilon_m + (1-p)\varepsilon_d \tag{4.2}$$

$$\varepsilon_\rho = \frac{\varepsilon_m \varepsilon_d}{(1-p)\varepsilon_m + p\varepsilon_d} \tag{4.3}$$

where ε_m and ε_d are the frequency-dependent permittivities of the metal and dielectric materials used in the multilayer. p represents the filling fraction of metal in the structure. If Cartesian coordinates are needed, the effective permittivity (ε_{xx}, ε_{xy}, ε_{yy}) of a hyperlens can be calculated according to [CPS$^+$06]. A multilayer hyperlens has negative permittivity in the ρ direction, and positive permittivity in the θ plane.

Choice of multilayer materials is an important step in the design process of the hyperlens. The conductive layer must support surface plasmon polaritons excitable by the illuminating light. In our case, using silver enabled operation towards the short-wavelength end of the visible spectrum, which is commonly used for both imaging and lithography purposes. Another key "lever" we can pull in our design process is the material we choose as our dielectric spacing layer. The desirable material properties should be low loss and a permittivity and refractive index that yield an effective medium with the desired dispersion relation.

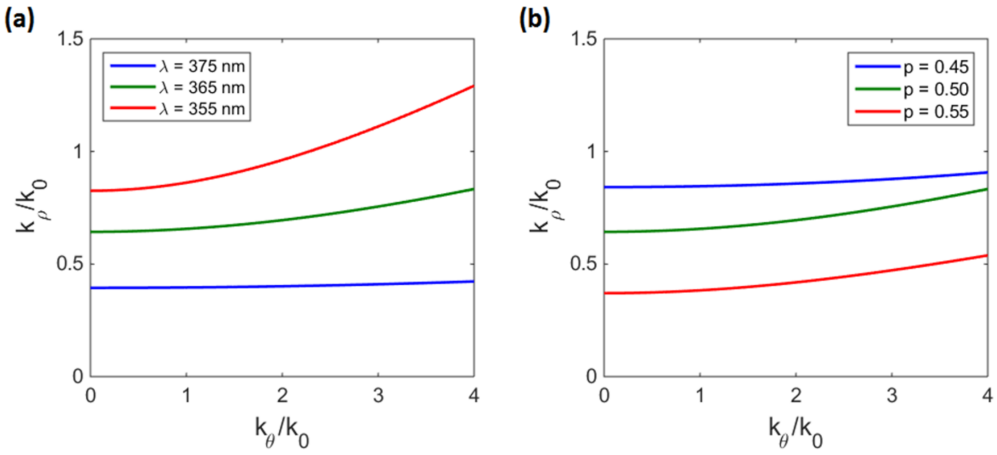

Figure 4.4: Hyperlens dispersion analysis: Analytically calculated isofrequency curves for different (a) wavelengths with a fixed metal filling factor ($p = 0.5$) and (b) filling factors with a fixed operational wavelength ($\lambda = 365$ nm) in various hyperlens designs.

In fact, the nature of the hyperbolic dispersion curve can be fairly sensitive to a number of parameters. Shown in Figs. 4.4(a),(b) is a series of isofrequency curves for a hyperlens with a single variable changed. It bears mentioning that at the operating frequency, a desirable dispersion curve should be broad and flat. When the slope is steeper, the wave will experience higher loss and the Poynting vector will be directed at an angle relative to the multilayer ρ axis.

A design parameter that should be delicately tuned in a hyperlens is the metal filling fraction. The relative percentage of metallic and dielectric materials has a strong effect on the material behavior. Dependent on each layer thickness, fabrication limits may also come into consideration. Physically, the dispersion relation will have a direct influence on the focusing and imaging performance of the hyperlens. The group velocity of propagating light in a medium is equal to the slope $\partial\omega/\partial k$, and the phase velocity is equal to the ratio ω/k. These two terms will dictate the phase, amplitude, and directionality of light passing through the hyperlens.

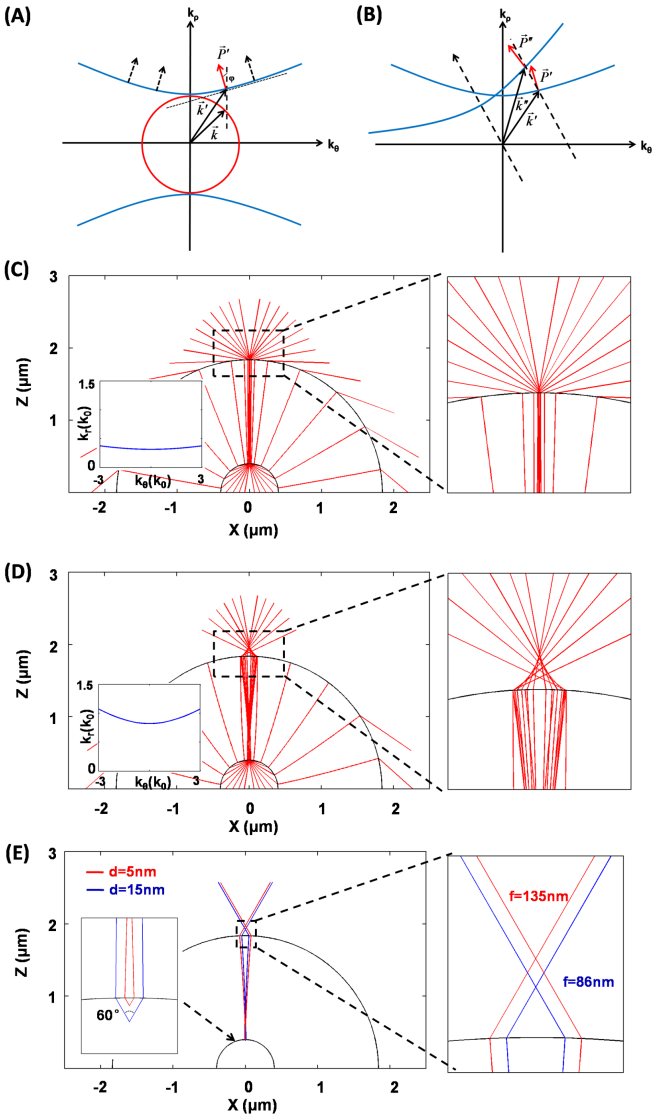

Figure 4.5: Ray tracing analysis: The hyperlens has a local dispersion based on the wavevector components in the θ and ρ directions for a ray entering and propagating within a hyperlens. (a) Poynting vector $\vec{P}'$ and wavevector $\vec{k}'$ for a ray entering a hyperlens (blue isofrequency curve) from a vacuum (red isofrequency curve). (b) $\vec{P}''$ and $\vec{k}''$ for a ray propagating within a hyperlens. Changes from $\vec{P}'$ and $\vec{k}'$ at the initial surface of the hyperlens are a result of the ray's changing orientation relative to the layer geometry during propagation. (c) and (d) show the ray tracing calculation for $\varepsilon_d = 2.6$ and $\varepsilon_d = 3.75$, respectively. The corresponding dispersions are shown in the inset. The radii of the inner and outer hyperlens layers were 400 nm and 1840 nm, respectively. The separation between the point source and the inner surface is set to d = 5 nm. (e) Ray tracing diagram illustrating the focusing behavior for different object positions with $\varepsilon_d = 3.75$. Only one pair of incident rays with equal angle is shown.

Based on a simplified ray-tracing analysis [JAN07], we can further analyze the design and functionality of the hyperlens. The Poynting vector $\vec{P}$ represents the directional electromagnetic energy flux density, and also gives us the directionality of a ray in a ray-tracing picture. In a low-loss scenario, the Poynting vector always points in a perpendicular direction to the isofrequency curve. Thus, in hyperbolic materials, $\vec{P}$ and $\vec{k}$ are usually not in parallel. Note that due to conservation of momentum, the wavevector component parallel to an interface is always conserved. Thus, if we know the initial k_θ, we can quickly calculate the angle φ that the Poynting vector makes with the $\hat{\rho}$ axis, starting from Eq. (4.1).

$$\tan(\varphi) = \frac{\partial k_\rho}{\partial k_\theta} = \frac{\varepsilon_\theta k_\theta}{\varepsilon_\rho k_\rho} = \frac{\varepsilon_\theta}{\varepsilon_\rho} \frac{k_\theta}{\sqrt{\varepsilon_\theta (k_0^2 + \frac{k_\theta}{\varepsilon_\rho})}} \tag{4.4}$$

Figure 4.5(a) illustrates the group velocity (in the Poynting vector $\vec{P}'$ direction) and phase velocity (in the wavevector $\vec{k}'$ direction) for a ray entering a hyperlens from a vacuum with initial wavevector $\vec{k}$. Note that the Poynting vector is parallel to $\vec{k}$ in the vacuum. Because the hyperlens has a curved multilayer geometry, rays with an initial incident angle will see changes in the local dispersion as they propagate inside of a hyperlens, since their orientation relative to the local coordinates will also be changing. This will affect the Poynting vector and the wavevector during propagation between the layers in a hyperlens, as shown in Fig. 4.5(b). The result from a ray-tracing perspective is a subtle bending of the ray path.

In Fig. 4.5(c),(d) we show how this ray tracing approach can be used to design the dispersion property of a hyperlens in order to optimize the material properties in our full wave simulations. Here, d is set to 5 nm, and p = 0.5. As an example, we change only one parameter, the permittivity of the dielectric layers. The result of this change is a change in the dispersion relation, which directly affects the ray tracing path. For ε_d = 2.6,

the isofrequency curve is quite flat. The light propagates almost completely along radial direction and forms a focal image at the outer interface. For ε_d = 3.75, we see a greater curvature in the dispersion, and a greater bending of the light. The rays are successfully focused at a point away from the outer surface of the hyperlens. It should be noted that the results in Fig. 4.5 are shown as a conceptual illustration; phase is not considered in this simplified model. We can clearly see that by altering the permittivity of the dielectric layers, we can dramatically change the focusing location of the hyperlens.

Interestingly in our imaging simulations, the focal position f gets closer to the hyperlens as the source position d gets farther away. We also calculated the path of a few rays with 30° off-axis angles, generating Fig. 4.5(e) for different source positions (5 nm and 15 nm). We note that the rays undergo a subtle bending as they travel through the hyperlens, a behavior which is dependent on the initial k_θ. We can see very clearly that the separation of the point source from the initial surface of the hyperlens will directly affect the focusing distance on the outer side. Matching with our COMSOL simulations, there is an inverse relationship observed between d and f.

4.4 Potential lithography applications

For an exploration of deeply sub-wavelength focusing with potential for application in lithography, simulations of a real hyperlens multilayer structure were conducted. Shown in Fig. 4.6(a) is the full wave simulation result and the real multilayer modeled geometry of the hyperlens. The inner surface of the hyperlens is assumed to be polished flat in this calculation. Alternating layers of silver (ε_{Ag} = -2.4 - 0.25i) and Al_2O_3 ($\varepsilon_{Al_2O_3}$ = 3.217) were used, with realistic material parameters [JC72][Pal98]. Each layer was 10 nm thick. The outermost layer had a radius of curvature of 1400 nm, and the innermost layer had a radius

of curvature of 600 nm. The illumination wavelength was chosen to be 365 nm, as this is an important wavelength in lithography applications.

Our time-reversal strategy involved two main steps. First, we calculated the far-fields detected through a hyperlens from a point source placed in the location we wish to use for lithography. The simplest design possesses a single spot below the center of the flat edge of the lens. Second, knowing the loss properties and geometry of the hyperlens, we can design a specific wavefront to send in the reverse direction to recreate the point source, or at least as small a spot as the hyperlens can manage. Because light propagates in the opposite direction, the spatial frequencies of the incoming wavefront are in fact increased dramatically, and so an otherwise unattainable sub-wavelength focus for lithography is realized.

Optical fabrication has many promising applications including creation of complex 3D extracellular microenvironments [ZQS$^+$12]. An extremely fine z-resolution was numerically demonstrated above for imaging. We can also achieve a similarly deep sub-wavelength z control in lithography, as shown in Figs. 4.6(b)-(d). By calculating the necessary wavefronts for different lithographic focus point positions, we can control the depth precisely. Because the hyperlens increases the k_θ component of light propagating in the radial direction, the focus spot will be tighter in all three dimensions than what would normally be achievable in a diffraction-limited setup.

The x-y resolution ability of the hyperlens is well established [MAL10][LL12]. In combination with the z performance shown in this work, we now can see the potential for three-dimensional super resolution imaging and lithography capability.

We have thus numerically demonstrated the super radial-resolution capability of hyperlenses, which has potential applications for 3D imaging and lithography within a thin volume close to the inner surface. Applications where visible-light super resolution is

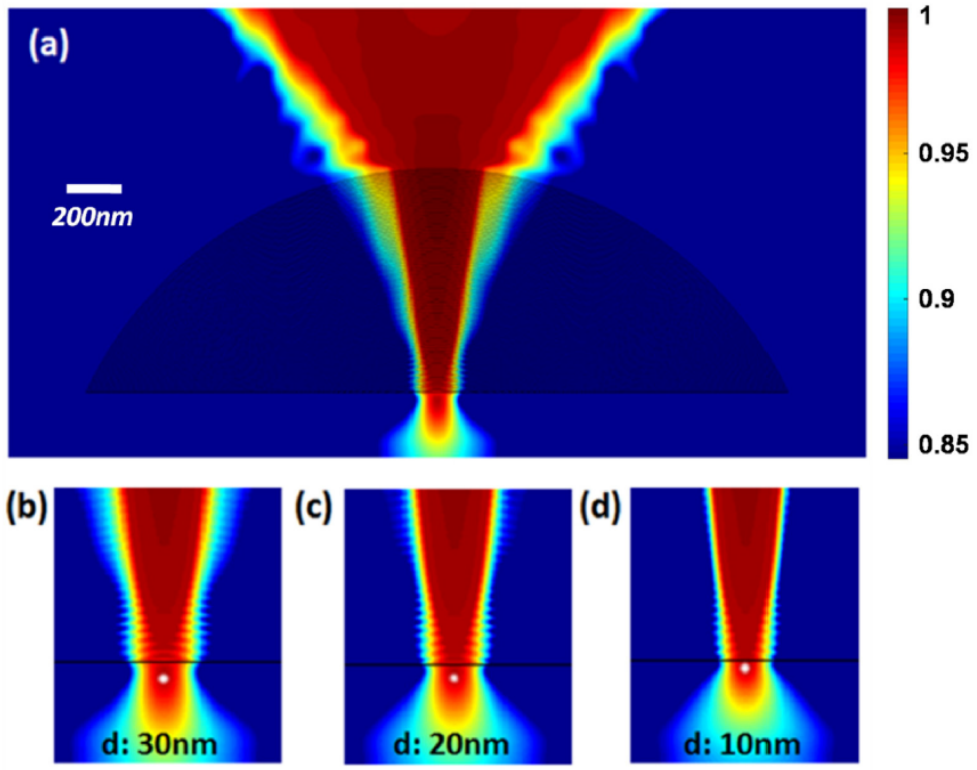

Figure 4.6: Hyperlens sub-wavelength focusing for lithography: (a) Multilayer structure for focusing ultraviolet light to a point using a hyperlens. The radii of the inner and outer hyperlens layers were 600 nm and 1400 nm, respectively. The normalized log-scale intensity is shown. The scale bar represents 200 nm. (b)-(d) Different distributions of amplitude and phase in three wavefronts sent towards the curved surface of the hyperlens result in three different focal z-depths. Note that *d* represents the spacing of the local maxima away from the hyperlens surface. This shows potential for very fine control of three-dimensional lithographic patterns. Note that the local maxima are highlighted with white color.

desired in conjunction with three dimensional capabilities are most obvious in biological fields. Since many sub-cellular and intracellular processes occur on the millisecond time scale, having high-speed potential is also attractive. Three-dimensional lithography and more generally scanning of a fine point of light with precise control could aid in a wide variety of patterning and manipulation tools.

There are some practical issues to be confronted with any multilayer hyperlens. Since the super resolution mechanism relies on the collection of evanescent fields, the sample of interest must be placed very close to the hyperlens. For objects thicker than several tens of nanometers, the evanescent decay will quickly become problematic. Despite this depth limitation, it should be feasible to fabricate (via lithography) or image larger 3D volumes using a layer-by-layer approach, similar to what is done in stereolithography [ZQS$^+$12] and 3D printing. With this approach, the final 3D structure height would be the individual layer depth multiplied by the number of layers. However, for certain applications, the combination of three-dimensional control and a strictly enforced and shallow z-range can be useful for eliminating unwanted background signal. These results hold promise for the development of hyperlenses with impressive 3D super resolution performance which avoid the typical sacrifices in speed and biological compatibility. Experimental implementation can be achieved without introducing prohibitive cost or complexity. As fabrication abilities continue to improve, new geometries and new possibilities will emerge. The 3D super resolution capability of the hyperlens shows great promise for a wide variety of exciting applications, although significant aspects still need further exploration, such as increasing the operational bandwidth, and enhancing experimental practicality.

Chapter 4, in part, is a reprint of the material as it appears in Optics Express, 2015, 23, 18501-18510. Weiwei Wan†, Joseph L. Ponsetto†, Zhaowei Liu, “Numerical study of

hyperlenses for three-dimensional imaging and lithography" [†Equal contribution]. The dissertation author was the co-first author of this paper.

Chapter 5

Conclusions and future work

In this work, new optical imaging techniques using plasmonics as a key physical mechanism have been introduced, demonstrated, and discussed at some length.

The LPSIM technique uses localized plasmons to translate a resonantly enhanced, finely structured near-field excitation pattern across an array of nano-antennas in parallel. It dramatically expands the super-resolving power of previous Structured Illumination Microscopy (SIM) by switching from simple laser interference patterns to localized plasmons as our source of structured illumination. Utilizing localized plasmons allows for fine near-field illumination structure which not only breaks the diffraction limit, but in fact is completely unchained from the dispersion curve of propagating light – a first for any SIM-based technique. With a straightforward image reconstruction process, high-quality imaging results are obtained for a variety of real fluorescent objects including relevant biological samples. A 3X resolution enhancement is achieved versus standard microscopy. Going forward, this technique may prove highly useful to biologists in the study of cellular and molecular activity in living organisms, especially where surface imaging is required. Because several aspects of this technique are scalable, there are many possibilities for future

application and improvement.

New LPSIM results not shown in this work suggest a clear path to 50 nm resolution of a biological sample by simply increasing the *NA* of the microscope objective. Video-rate imaging speed is also demonstrable for bright biological samples, using commercially available CMOS cameras with high frame rates.

This work also shows new capabilities of the hyperlens. For super resolution, the evanescent object fields must come into contact with the hyperlens surface before exponential decay becomes problematic. However, within a thin volume close to the hyperlens, three dimensional super resolution imaging is possible. In full wave imaging simulations, it is shown that axial object localization accuracy down to just five nanometers is possible via far-field detection, in addition to the lateral super resolution commonly expected of the hyperlens. Using a time-reversal approach, it is also shown that a carefully designed wavefront sent backwards through the hyperlens can create a sub-wavelength focus point, and the axial depth can be controlled with similar accuracy down to five nanometers. Ray tracing analysis is used to analyze the underlying physical picture for light passing both ways through a hyperlens. This understanding guides an optimization of our hyperlens structure based on the parameters affecting the hyperbolic dispersion such as operating wavelength, metal filling fraction, and dielectric layer permittivity. This work demonstrates promising potential for applications requiring three dimensional super resolution in either imaging, lithography, or both, at optical frequencies.

The differences between plasmons and photons as carriers of optical information can be exploited in a multitude of ways, and can lead to significant advances in science.

Appendix A

MATLAB reconstruction code

```
%%%%% BLIND LPSIM/PSIM EXPERIMENTAL RECONSTRUCTION CODE
%%% By Joe Ponsetto
%%% Run with fconv2 in the same folder.

clearvars; clc; format compact; close all;
tic;

%%% Specify sub-image files
filepath = 'C:\Users\jlpon\Dropbox\Data\LPSIM_images\d';
SubIms(:,:,1) = importdata([filepath '0001.asc']);
SubIms(:,:,2) = importdata([filepath '0002.asc']);
SubIms(:,:,3) = importdata([filepath '0003.asc']);
SubIms(:,:,4) = importdata([filepath '0004.asc']);
SubIms(:,:,5) = importdata([filepath '0005.asc']);
SubIms(:,:,6) = importdata([filepath '0006.asc']);
```

```
SubIms(:,:,7) = importdata([filepath '0007.asc']);
SubIms(:,:,8) = importdata([filepath '0008.asc']);
SubIms(:,:,9) = importdata([filepath '0009.asc']);
SubIms = SubIms(:,2:end,:); % clean .asc file
L = size(SubIms,3); % number of sub-images used

%%% Specify some reconstruction parameters
N_iter = 100; % number of iterations to run
ls_iter = 20; % maximum line search sub-iterations
c1_step = 5; % larger --> better line search
int_fac = 5; % interpolation factor
m = 800; % reconstructed image size (post-interpolation)
r_top = 50; % topmost row to reconstruct
c_left = 50; % leftmost column to reconstruct
descent = 2; % 1: gradient; 2: conjugate gradient
desdir = 2; % 1: new; 2: old
align_im = 0; % 1: align sub-images
i_mod = 1; % intensity multiplier
if align_im == 1
    pxmin = 0; pxmax = 0; % define peak search pixel box
    pymin = 0; pymax = 0;
end
nr = 1; % 1: mitigate noise
if nr == 1
```

```
    nymin = 10; nymax = 30; % define noise background box
    nxmin = 10; nxmax = 30;
    f_wien = 0; % 1: weiner filter smoothing
    f_p = 3; % filter parameter
end

%%% Specify some experimental parameters
NA = 1.2; % numerical aperture
mag = 60*4; % optical magnification
wavelength = 500; % fluorescence WL [nm]
campix = 16000; % CCD real pixel size [nm]
mag_pix = campix/mag; % magnified effective hardware pixel
   size [nm]
pixelsize = mag_pix/int_fac; % pixel size [nm] after
   interpolation

SubIms = i_mod*SubIms; % increase photon count for better
   reconstruction

%%% Align sub-images automatically with a designated marker
if align_im == 1
    search_1 = SubIms(pymin:pymax,pxmin:pxmax,1); ssize =
       size(search_1);
        [~,max_ind] = max(search_1(:)); % find peak in first
```

```
            sub-image
        [max_row,max_col] = ind2sub(ssize,max_ind);
    for ind_sub = 2:L
        search_m = SubIms(pymin:pymax,pxmin:pxmax,ind_sub);
        [~,max_ind_i] = max(search_m(:));
        [max_row_i,max_col_i] = ind2sub(ssize,max_ind_i);
        shift_ud = max_row - max_row_i; shift_lr = max_col -
            max_col_i;
        SubIms(:,:,ind_sub) = ...
            circshift(SubIms(:,:,ind_sub),[shift_ud shift_lr
               ]);
    end
end
figure(80); imagesc(mean(SubIms,3)); axis image; colormap(
   hot(256));
title('Averaged diffraction-limited raw images (full)');
set(gca,'fontsize',15);

%%% Crop image area
crop_dim = round((m*pixelsize)/mag_pix); % m*pixelsize =
   dimension [nm]
c_right = c_left + crop_dim; r_bottom = r_top + crop_dim;
CropIms = SubIms(r_top:r_bottom,c_left:c_right,:);
```

```
%%% Mitigate noise
figure(81);
subplot(1,2,1); imagesc(CropIms(:,:,2));
title('CCD data'); colormap(hot); axis image;
if nr == 1
%     if f_wien == 1
        for ind_nr = 1:L
            CropIms(:,:,ind_nr) = wiener2(CropIms(:,:,ind_nr
               ),[f_p f_p]);
        end
%     end
    BGC = zeros(size(CropIms));
    for ind_bg = 1:L
        bg_sub = mean2(CropIms(nymin:nymax,nxmin:nxmax,
           ind_bg));
        BGC(:,:,ind_bg) = CropIms(:,:,ind_bg) - .80*bg_sub;
    end
    BGC(BGC<0) = 0; CropIms = BGC;
end
subplot(1,2,2); imagesc(CropIms(:,:,2));
title('Noise reduction'); colormap(hot); axis image;

%%% Interpolate image area
InterpIms = imresize(CropIms, [m m], 'bicubic');
```

```
InterpIms(InterpIms<0) = 0; % correct for interpolation
   overshoot
f82 = figure(82); set(f82,'units','normalized','
   outerposition',[0 0 1 1]);
colormap(hot(256));
for ind_plot = 1:L
    subplot(3,3,ind_plot); imagesc(InterpIms(:,:,ind_plot));
    title(['sub-im_' num2str(ind_plot)]);
    axis image; axis off; colorbar; set(gca,'fontsize',13);
end
sup82 = suptitle(['Raw sub-images (L = ' num2str(L) ')']);
set(sup82,'FontSize',18);

%%% Define PSF
L1 = (0.61*wavelength/NA)/pixelsize; % pixels within
   Rayleigh criterion
u = floor(L1)-2;
[Xpsf,Ypsf] = meshgrid(-u:u,-u:u);
R = sqrt(Xpsf.^2 + Ypsf.^2); % polar r-coordinate
R = R*1.220*pi/L1;
psf = (2*besselj(1,R)./R).^2; psf(u+1,u+1)=1;
psf = psf/sum(psf(:));

%%% Zero-pad sub-images
```

```
z_edge = 2*ceil(L1);
mzp = m + z_edge;
M = zeros(mzp,mzp,L); r_x = M;
M(1+z_edge/2:z_edge/2+m,1+z_edge/2:z_edge/2+m,1:L) =
   InterpIms;

%%% Define initial guesses [M - Ip*h]
X0 = zeros(mzp,mzp,L); % tensor holding initial guesses
obj = sum(M,3)/L;
objcoeff = round(sqrt(max(obj(:))));
obj = objcoeff*obj/max(obj(:)); mean_obj = mean2(obj);
X0(:,:,1) = obj; % initial guess at object
X0(1:z_edge/2,:,1) = mean_obj;
X0(z_edge/2+m+1:end,:,1) = mean_obj;
X0(:,1:z_edge/2,1) = mean_obj;
X0(:,z_edge/2+m+1:end,1) = mean_obj;
X0(:,:,2:L) = ones(mzp,mzp,L-1).*objcoeff; % SIP guesses
I0 = ones(mzp,mzp)*objcoeff; % initial guess at average
   illumination

%%% Define edge mask for cost function evaluation
maskc = zeros(mzp,mzp);
maskc(1+z_edge/2:z_edge/2+m,1+z_edge/2:z_edge/2+m) = 1;
maskcm = repmat(maskc,1,1,L);
```

```
%%% Initiate iteration parameters
alpha0 = 1e-5;
gamma  = zeros(1,L);
gammat = gamma;
g = zeros(mzp,mzp,L);
d = g; dp = g;
F_x = zeros(N_iter,1);
alcoef = zeros(N_iter,1);
gammacoef = zeros(N_iter,L);
fcost = zeros(N_iter,2);
c1t = [0.9,0.9,0.2,0.2,0.01,0.01,0.001,0.001,1e-4];
X = sqrt(X0); % sqrt used to enforce positivity constraint

%% Iterative reconstruction

for k = 1:N_iter
    c1 = c1t(min(floor((k-1)/c1_step)+1,length(c1t)));
    X_obj = X(:,:,1).^2;

    f83 = figure(83);
    set(f83, 'units','normalized','outerposition',[0 0 1 1])
    subplot(2,2,1); imagesc(X0(:,:,1)); axis off; axis image
       ; colorbar;
```

```
title('Initial guess');
subplot(2,2,2); imagesc(X_obj); axis off; axis image;
   colorbar;
title(['Reconstructed object (k = ' num2str(k) ')']);
subplot(2,2,3); imagesc(X(:,:,2).^2); axis off; axis
   image; colorbar;
title('SIP_1 estimate');
subplot(2,2,4); imagesc(X(:,:,L).^2); axis off; axis
   image; colorbar;
title('SIP_L estimate');
sup83 = suptitle('Iterative reconstruction progress');
set(sup83,'FontSize',18);
drawnow;
if mod(k,10) == 0
    checkfig = figure; imagesc(X_obj);
    axis off; axis image; colorbar;
    title(['Result after ' num2str(k) ' iterations']);
end

%%% Calculate residual error
for ind_rx = 1:L-1
    r_x(:,:,ind_rx) = M(:,:,ind_rx) - ...
        fconv2(X_obj.*(X(:,:,ind_rx + 1).^2),psf).*maskc
           ;
```

```
end
Isum = sum(X(:,:,2:L).^2,3);
XF = L*I0 - Isum;
r_x(:,:,L) = M(:,:,L) - fconv2(X_obj.*XF,psf).*maskc;

%%% Define cost function
F_2d = sum(abs(r_x).^2,3);
F_x(k) = sum(F_2d(:)); % total cost: sum of cost in each
    pixel

%%% Define gradients
g_obj = 0;
for ind_gr = 1:L-1
    g_obj = g_obj + ((X(:,:,ind_gr + 1).^2).*X(:,:,1)).*
       fconv2(r_x(:,:,ind_gr),psf);
end
g_obj = g_obj + XF.*X(:,:,1).*fconv2(r_x(:,:,L),psf);
g(:,:,1) = g_obj;
for ind_g = 2:L
    g(:,:,ind_g) = ...
        (X_obj.*X(:,:,ind_g)).*fconv2(r_x(:,:,ind_g-1)-
           r_x(:,:,L),psf);
end
if descent == 1 %%% gradient
```

```
    d = g;
    f_15 = ' [Grad. descent]';
elseif descent == 2 %%% conjugate gradient
    f_15 = ' [Conj. grad. descent]';
    for ind_cg = 1:L
        if k ~= 1
            gamma(ind_cg) = ...
                sum(sum(g(:,:,ind_cg).*(g(:,:,ind_cg)-gp
                   (:,:,ind_cg))))...
                /sum(sum(gp(:,:,ind_cg).^2));
        end
    end

    %%% Guarantee descent direction
    if desdir == 1
        gamma(gamma<0) = 0;
    end
    if min(gamma) < 0
        gamma = zeros(1,L);
    end

    for ind_d = 1:L
        d(:,:,ind_d) = g(:,:,ind_d)+gamma(ind_d)*dp(:,:,
           ind_d);
```

```
    end
    dp = d; gp = g;
end
gammacoef(k,:) = gamma;

%%% Find alpha
alpha = alpha0;
gsum = sum(sum(sum(-d.*g.*maskcm))); % scale to matrix
   magnitude
for ls_count = 1:ls_iter
    minimprove = F_x(k) + c1*alpha*gsum;
    Xt = X + alpha*d;
    %%% re-calculate cost function
    F_rc = 0; XFi = L*I0;
    for ind_cf = 1:L-1
        F_rc = F_rc + (abs((M(:,:,ind_cf) - ...
            fconv2((Xt(:,:,1).^2).*(Xt(:,:,ind_cf + 1)
               .^2),psf)).*maskc).^2);
        XFi = XFi - Xt(:,:,ind_cf+1).^2;
    end
    F_rc = F_rc + (abs((M(:,:,L) - ...
        fconv2((Xt(:,:,1).^2).*XFi,psf)).*maskc).^2);
    f1 = sum(sum(F_rc));
    if f1 <= minimprove
```

```
            break
        else
            alpha = alpha/2;
        end
    end
    alcoef(k) = alpha;
    fcost(k,:) = [f1 minimprove];

    %%% Update X
    X = X + alpha*d;
end

%%% Select reconstructed image
re = X(1+z_edge/2:z_edge/2+m,1+z_edge/2:z_edge/2+m,1).^2;

%% Plot reconstruction parameters

parfig = figure(25);
set(parfig, 'units','normalized','outerposition',[0 0 1 1]);
subplot(2,2,1); semilogy(alcoef,'LineWidth',2); xlabel('
   Iteration #'); ylabel('\alpha');
title(['\alpha-coefficient' f_15]); set(gca,'fontsize',13);
subplot(2,2,2); imagesc(flip(rot90(gammacoef)));
xlabel('Iteration #'); ylabel('Object / SIP matrix');
```

```
colorbar; title('\gamma-coefficient'); set(gca,'fontsize'
   ,13);
subplot(2,2,3); semilogy(fcost(:,1),'r','LineWidth',2); hold
    on;
semilogy(fcost(:,2),'b','LineWidth',2); set(gca,'fontsize'
   ,13);
legend('Reduced CF','Max Allowed'); xlabel('Iteration #');
   ylabel('Cost');
title('Convergence');
ax = subplot(2,2,4);
toc15 = num2str(round(toc,2));
PctR15 = num2str(round(100*(F_x(end-1)-F_x(end))/F_x(end),2)
   );
text(0.1,0.6,...
    {['Reconstruction time: ' toc15 ' s'];...
    [];['Last iteration cost reduction: ' PctR15 '%']},'
       FontSize',15);
set (ax,'visible','off')

%% Plot reconstruction result

resfig = figure(26);
set(resfig, 'units','normalized','outerposition',[0 0 1 1]);
im0 = sum(InterpIms,3)/L;
```

```
im0_N = im0/max(max(im0));
re_N = re/max(max(re));
colormap(hot(256));
subplot(1,2,1); s9 = pixelsize/2;
imagesc((1e-3)*[s9 pixelsize*(m-1)+s9],(1e-3)*[s9 pixelsize
   *(m-1)+s9],im0_N);
colorbar; axis image; set(gca,'fontsize',15);
title('Diffraction-limited image');
xlabel('x position [\mum]'); ylabel('y position [\mum]');
subplot(1,2,2);
imagesc((1e-3)*[s9 pixelsize*(m-1)+s9],(1e-3)*[s9 pixelsize
   *(m-1)+s9],re_N);
colorbar; axis image; set(gca,'fontsize',15);
title('LPSIM super resolution image');
xlabel('x position [\mum]'); ylabel('y position [\mum]');
sup17 = suptitle('Reconstruction result'); set(sup17,'
   FontSize',20);

%% Plot Fourier transform

contrast_f = 1; % 0: none; 1: 0-min;
cimin = 0.70; cimax = 0.95;
crmin = 0.70; crmax = 0.95;
f_i = 8; % interpolation factor
```

```
fftfig = figure(27);
set(fftfig, 'units','normalized','outerposition',[0 0 1 1]);
im0_Nf = im0_N; re_Nf = re_N;
f_im0 = log(abs(ifftshift(fft2(im0_Nf))));
f_re = log(abs(ifftshift(fft2(re_Nf))));
if contrast_f == 1
        min_im = min(min(f_im0)); max_im = max(max(f_im0));
           % find min and max
    min_re = min(min(f_re)); max_re = max(max(f_re));
    zshift_im = abs(min([0 min_im])); % get log scale with 0
        as min
    zshift_re = abs(min([0 min_re]));
    f_im0 = (f_im0 + zshift_im);
    f_re = (f_re + zshift_re);
    max_fz_im = max_im + zshift_im; max_fz_re = max_re +
       zshift_re;
    min_fz_im = min_im + zshift_im; min_fz_re = min_re +
       zshift_re;
    C_txt_im0 = ',[cimin*max_fz_im cimax*max_fz_im]';
    C_txt_re = ',[crmin*max_fz_re crmax*max_fz_re]';
else
    C_txt_im0 = '';
    C_txt_re = '';
end
```

```
a_fac = 0.5; am = round(a_fac*m); a_width = m*pixelsize; %
   FOV [nm]
a_c = (1 + round((m/2)-(am/2))):round((m/2)+(am/2)); % look
   at low-k features
f_im0_c = f_im0(a_c,a_c);
f_re_c = f_re(a_c,a_c);
f_im0_i = imresize(f_im0_c, f_i, 'bicubic');
f_re_i = imresize(f_re_c, f_i, 'bicubic');
sf = size(f_im0_i); [Xm,Ym] = meshgrid(-sf/2:sf/2-1, -sf/2:
   sf/2-1);
k0 = 2*pi/wavelength; % [rad/nm]
fxy = 2*pi*(round(-am/2):round(am/2))/a_width; % [radians
   per aperture width]
kxy = fxy/k0; % [k/k0]
subplot(1,2,1);
eval(['imagesc(kxy, kxy, f_im0_i' C_txt_im0 ')']);
axis image; set(gca,'fontsize',15); xlabel('k_x/k_0');
   ylabel('k_y/k_0');
title('Diffraction-limited spatial frequencies');
subplot(1,2,2);
eval(['imagesc(kxy, kxy, f_re_i' C_txt_re ')']);
axis image; set(gca,'fontsize',15); xlabel('k_x/k_0');
   ylabel('k_y/k_0');
title('LPSIM spatial frequencies');
```

```
sup18 = suptitle('Fourier transform comparison'); set(sup18,
   'FontSize',20);

%% 1D intensity comparison plot

deg = 0; % positive: CCW
col_prof = 143; % [X]
row_profi = 247; % [Y]
i_fac = 2;
proffig = figure(28);
set(proffig, 'units','normalized','outerposition',[0 0 1 1])
   ;
im0_rot = imrotate(im0,deg,'nearest','loose');
re_rot = imrotate(re,deg,'nearest','loose');
subplot(1,2,1); imagesc(re_rot); axis image; title('Rotated
   reconstructed image')
colormap hot(256);
subplot(1,2,2);
im_line = im0_rot(row_profi,:);
im_line = interp(im_line,i_fac);
im_line = im_line/max(im_line);
re_line = re_rot(row_profi,:);
re_line = interp(re_line,i_fac);
re_line = re_line/max(re_line);
```

```
x_i = pixelsize*(1e-3)*(1:length(im_line))/i_fac;
x_r = pixelsize*(1e-3)*(1:length(re_line))/i_fac;
plot(x_i,im_line,'b','LineWidth',3); hold on;
plot(x_r,re_line,'r','LineWidth',3); hold off;
set(gca,'fontsize',15); xlabel('Position [\mum]');
ylabel('Intensity [A.U.]');
legend('Diffraction-limited','LPSIM');

toc;
```

Appendix B

MATLAB experimental automation code

```
%%%%% LPSIM EXPERIMENTAL DAQ --> MIRROR/CAMERA
%%% By Joe Ponsetto

clearvars; clc; format compact;

%%% Experimental parameters
x_offset = 0; % voltage offset [V]
y_offset = 0;
a1o = 0; a2o = 0; a3o = 0; % angle offset [deg] (positive:
   CW)
max_ang = 50; % [deg]
ang_step = 25; % [deg]
t_exp = .05; % [s]

%%% Initialize DAQ
```

```
daqregister('mcc');
MCC_Info = daqhwinfo('mcc');
Construct_Names = daqhwinfo('mcc','ObjectConstructorName');
pause(.2);

%% Prepare output

%%% Set voltages:
% (0.5 V per mechanical degree)
% (0.25 V per theta_1 optical degree)
theta_2 = -max_ang:ang_step:max_ang; % [deg]
theta_1 = atand((1.5/5.5)*tand(theta_2));
V_t = 0.25*theta_1; % [V]
v1 = 0; v2 = 60; v3 = 60;
V_a1 = [V_t*sind(v1 + a1o); V_t*cosd(v1 + a1o)]';
V_a2 = [V_t*sind(v2 + a2o); V_t*cosd(v2 + a2o)]';
V_a3 = [V_t*sind(v3 + a3o); -V_t*cosd(v3 + a3o)]';
V_xy = [V_a1; V_a2; V_a3];
V_xy(:,1) = V_xy(:,1) + x_offset; V_xy(:,2) = V_xy(:,2) +
   y_offset;
l_seq = length(V_xy);

%%% Initialize output channel
ao = analogoutput( 'mcc', 0 );
```

```
addchannel(ao,[0 1 2]);
% NOTE:       [X Y CCD]

%% Run experiment

tic;
%%% Send output voltages
putsample(ao,[x_offset y_offset 0]); pause(.1); % zero
   initial voltages

% CCD trigger defined by rising edge
V_c = 5; % [V]
for ind_V = 1:l_seq
    V_m = [V_xy(ind_V,:), 0];
    putsample(ao,V_m); % set mirrors
    V_out = [V_xy(ind_V,:), V_c];
    putsample(ao,V_out); pause(t_exp); % trigger camera
end
putsample(ao,[0 0 0]); % zero final voltages
toc;
```

Bibliography

[AC77] Grant M. Albrecht and J. Alan Creighton. Anomalously intense Raman spectra of pyridine at a silver electrode. *Journal of the American Chemical Society*, 99(15):5215–5217, 1977.

[AN72] E. A. Ash and G. Nicholls. Super-resolution aperture scanning microscope. *Nature*, 237(5357):510–512, 1972.

[Axe01] Daniel Axelrod. Total internal reflection fluorescence microscopy in cell biology. *Traffic*, 2(11):764–774, 2001.

[Bar98] W. L. Barnes. Fluorescence near interfaces: the role of photonic mode density. *Journal of Modern Optics*, 45(4):661–699, 1998.

[BDE03] William L. Barnes, Alain Dereux, and Thomas W. Ebbesen. Surface plasmon subwavelength optics. *Nature*, 424(6950):824–830, 2003.

[BLZ09] Guy Bartal, Geoffroy Lerosey, and Xiang Zhang. Subwavelength dynamic focusing in plasmonic nanostructures using time reversal. *Physical Review B*, 79(20):201103, 2009.

[BPS+06] Eric Betzig, George H. Patterson, Rachid Sougrat, O. Wolf Lindwasser, Scott Olenych, Juan S. Bonifacino, Michael W. Davidson, Jennifer Lippincott-Schwartz, and Harald F. Hess. Imaging intracellular fluorescent proteins at nanometer resolution. *Science*, 313(5793):1642–1645, 2006.

[BW99] Max Born and Emil Wolf. *Principles of Optics*. Cambridge University Press, 1999.

[CPS+06] Steven A. Cummer, Bogdan-Ioan Popa, David Schurig, David R. Smith, and John B. Pendry. Full-wave simulations of electromagnetic cloaking structures. *Physical Review E*, 74(3):036621, 2006.

[CSP+13] Elizabeth P. Canović, D. Thomas Seidl, Samuel R. Polio, Assad A. Oberai, Paul E. Barbone, Dimitrije Stamenović, and Michael L. Smith. Biomechanical imaging of cell stiffness and prestress with subcellular resolution. *Biomechanics and Modeling in Mechanobiology*, 13(3):665–678, 2013.

[CW09] Lin Chen and Guo P. Wang. Pyramid-shaped hyperlenses for three-dimensional subdiffraction optical imaging. *Optics Express*, 17(5):3903–3912, 2009.

[Deu16] Miriam Deutsch. Multiscale thin metal films for enhanced sensing and light harvesting applications. reu.uoregon.edu/research-projects, 2016. Accessed: 2016-08-10.

[DH02] Marcus Dyba and Stefan W. Hell. Focal spots of size λ/23 open up far-field fluorescence microscopy at 33 nm axial resolution. *Physical Review Letters*, 88(16):163901, 2002.

[DKF+02] H. Ditlbacher, J. R. Krenn, N. Felidj, B. Lamprecht, G. Schider, M. Salerno, A. Leitner, and F. R. Aussenegg. Fluorescence imaging of surface plasmon fields. *Applied Physics Letters*, 80(3):404–406, 2002.

[DLSZ06] Stéphane Durant, Zhaowei Liu, Jennifer M. Steele, and Xiang Zhang. Theory of the transmission properties of an optical far-field superlens for imaging beyond the diffraction limit. *Journal of the Optical Society of America B*, 23(11):2383–2392, 2006.

[Dru00] Paul Drude. Zur elektronentheorie der metalle. *Annalen der Physik*, 306(3):566–613, 1900.

[FDLP15] Antonio I. Fernández-Domínguez, Zhaowei Liu, and John B. Pendry. Coherent four-fold super-resolution imaging with composite photonic-plasmonic structured illumination. *ACS Photonics*, 2(3):341–348, 2015.

[FLSZ05] Nicholas Fang, Hyesog Lee, Cheng Sun, and Xiang Zhang. Sub-diffraction-limited optical imaging with a silver superlens. *Science*, 308(5721):534–537, 2005.

[FSR+12] Reto Fiolka, Lin Shao, E. Hesper Rego, Michael W. Davidson, and Mats G. L. Gustafsson. Time-lapse two-color 3D imaging of live cells with doubled resolution using structured illumination. *Proceedings of the National Academy of Sciences*, 109(14):5311–5315, 2012.

[FWMDN09] Carlo Forestiere, Gary F. Walsh, Giovanni Miano, and Luca Dal Negro. Nanoplasmonics of prime number arrays. *Optics Express*, 17(26):24288–24303, 2009.

[GAJ+13] B. Gjonaj, J. Aulbach, P. M. Johnson, A. P. Mosk, L. Kuipers, and A. Lagendijk. Focusing and scanning microscopy with propagating surface plasmons. *Physical Review Letters*, 110(26):266804, 2013.

[Gar07] Rafael Garcia. Electrons flowing in a metal according to drude model. commons.wikimedia.org/wiki/File:Electrona_in_crystallo_fluentia.png, 2007. Accessed: 2016-08-08.

[GAS00] Mats G. L. Gustafsson, David A. Agard, and John W. Sedat. Doubling the lateral resolution of wide-field fluorescence microscopy using structured illumination. *SPIE*, 3919:141–150, 2000.

[GSC+12] J. Girard, G. Scherrer, A. Cattoni, E. Le Moal, A. Talneau, B. Cluzel, F. de Fornel, and A. Sentenac. Far-field optical control of a movable subdiffraction light grid. *Physical Review Letters*, 109(18):187404, 2012.

[Gus00] Mats G. L. Gustafsson. Surpassing the lateral resolution limit by a factor of two using structured illumination microscopy. *Journal of Microscopy*, 198(2):82–87, 2000.

[Gus05] Mats G. L. Gustafsson. Nonlinear structured-illumination microscopy: wide-field fluorescence imaging with theoretically unlimited resolution. *Proceedings of the National Academy of Sciences*, 102(37):13081–13086, 2005.

[GZF05] Javier García, Zeev Zalevsky, and Dror Fixler. Synthetic aperture superresolution by speckle pattern projection. *Optics Express*, 13(16):6073–6078, 2005.

[HC99] Rainer Heintzmann and Christoph G. Cremer. Laterally modulated excitation microscopy: improvement of resolution by using a diffraction grating. *SPIE*, 3568:185–196, 1999.

[HJC02] Rainer Heintzmann, Thomas M. Jovin, and Christoph Cremer. Saturated patterned excitation microscopy – a concept for optical resolution improvement. *Journal of the Optical Society of America A*, 19(8):1599–1609, 2002.

[HSW+00] Bert Hecht, Beate Sick, Urs P. Wild, Volker Deckert, Renato Zenobi, Olivier J. F. Martin, and Dieter W. Pohl. Scanning near-field optical microscopy with aperture probes: fundamentals and applications. *The Journal of Chemical Physics*, 112(18):7761–7774, 2000.

[Huy78] Christiaan Huygens. *Traité de la Lumière*. Van der Aa, 1678.

[HW94] Stefan W. Hell and Jan Wichmann. Breaking the diffraction resolution limit by stimulated emission: stimulated-emission-depletion fluorescence microscopy. *Optics Letters*, 19(11):780–782, 1994.

[HZS+05] Erin M. Hicks, Shengli Zou, George C. Schatz, Kenneth G. Spears, Richard P. Van Duyne, Linda Gunnarsson, Tomas Rindzevicius, Kasemo Bengt, and Mikael Käll. Controlling plasmon line shapes through diffractive coupling in linear arrays of cylindrical nanoparticles fabricated by electron beam lithography. *Nano Letters*, 5(6):1065–1070, 2005.

[JAN06] Zubin Jacob, Leonid V. Alekseyev, and Evgenii Narimanov. Optical hyperlens: far-field imaging beyond the diffraction limit. *Optics Express*, 14(18):8247–8256, 2006.

[JAN07] Zubin Jacob, Leonid V. Alekseyev, and Evgenii Narimanov. Semiclassical theory of the hyperlens. *Journal of the Optical Society of America A*, 24(10):A52–A59, 2007.

[JC72] Peter B. Johnson and R. W. Christy. Optical constants of the noble metals. *Physical Review B*, 6(12):4370–4379, 1972.

[JVD77] David L. Jeanmaire and Richard P. Van Duyne. Surface Raman spectroelectrochemistry: part I. heterocyclic, aromatic, and aliphatic amines adsorbed on the anodized silver electrode. *Journal of Electroanalytical Chemistry*, 84(1):1–20, 1977.

[KBL96] Vijay Krishnamurthi, Brent Bailey, and Frederick Lanni. Image processing in 3-D standing-wave fluorescence microscopy. *SPIE*, 2655:18–25, 1996.

[KCG+09] Peter Kner, Bryant B. Chhun, Eric R. Griffis, Lukman Winoto, and Mats G. L. Gustafsson. Super-resolution video microscopy of live cells by structured illumination. *Nature Methods*, 6(5):339–342, 2009.

[KCN+10] Ondrej L. Krivanek, Matthew F. Chisholm, Valeria Nicolosi, Timothy J. Pennycook, George J. Corbin, Niklas Dellby, Matthew F. Murfitt, Christopher S. Own, Zoltan S. Szilagyi, Mark P. Oxley, Sokrates T. Pantelides, and Stephen J. Pennycook. Atom-by-atom structural and chemical analysis by annular dark-field electron microscopy. *Nature*, 464(7288):571–574, 2010.

[KCZS03] K. Lance Kelly, Eduardo Coronado, Lin Lin Zhao, and George C. Schatz. The optical properties of metal nanoparticles: the influence of size, shape, and dielectric environment. *The Journal of Physical Chemistry B*, 107(3):668–677, 2003.

[KSG08] V. G. Kravets, F. Schedin, and A. N. Grigorenko. Extremely narrow plasmon resonances based on diffraction coupling of localized plasmons in arrays of metallic nanoparticles. *Physical Review Letters*, 101(8):087403, 2008.

[KSS+10] Philipp J. Keller, Annette D. Schmidt, Anthony Santella, Khaled Khairy, Zhirong Bao, Joachim Wittbrodt, and Ernst H. K. Stelzer. Fast, high-contrast imaging of animal development with scanned light sheet-based structured-illumination microscopy. *Nature Methods*, 7(8):637–642, 2010.

[LCS+09] S. Liu, Chin-Jung Chuang, C. W. See, G. Zoriniants, W. L. Barnes, and M. G. Somekh. Double-grating-structured light microscopy using plasmonic nanoparticle arrays. *Optics Letters*, 34(8):1255–1257, 2009.

[LDL+07] Zhaowei Liu, Stéphane Durant, Hyesog Lee, Yuri Pikus, Nicolas Fang, Yi Xiong, Cheng Sun, and Xiang Zhang. Far-field optical superlens. *Nano Letters*, 7(2):403–408, 2007.

[LdRTF07] Geoffroy Lerosey, Julien de Rosny, Arnaud Tourin, and Mathias Fink. Focusing beyond the diffraction limit with far-field time reversal. *Science*, 315(5815):1120–1122, 2007.

[LKW+03] Stefan Lakämper, Athina Kallipolitou, Günther Woehlke, Manfred Schliwa, and Edgar Meyhöfer. Single fungal kinesin motor molecules move processively along microtubules. *Biophysical Journal*, 84(3):1833–1843, 2003.

[LL12] Dylan Lu and Zhaowei Liu. Hyperlenses and metalenses for far-field superresolution imaging. *Nature Communications*, 3:1205, 2012.

[LLX+07a] Hyesog Lee, Zhaowei Liu, Yi Xiong, Cheng Sun, and Xiang Zhang. Development of optical hyperlens for imaging below the diffraction limit. *Optics Express*, 15(24):15886–15891, 2007.

[LLX+07b] Zhaowei Liu, Hyesog Lee, Yi Xiong, Cheng Sun, and Xiang Zhang. Far-field optical hyperlens magnifying sub-diffraction-limited objects. *Science*, 315(5819):1686–1686, 2007.

[LSC+15] Dong Li, Lin Shao, Bi-Chang Chen, Xi Zhang, Mingshu Zhang, Brian Moses, Daniel E. Milkie, Jordan R. Beach, John A. Hammer, Mithun Pasham, Tomas Kirchhausen, Michelle A. Baird, Michael W. Davidson, Pingyong Xu, and Eric Betzig. Extended-resolution structured illumination imaging of endocytic and cytoskeletal dynamics. *Science*, 349(6251):aab3500, 2015.

[Mai07] Stefan A. Maier. *Plasmonics: Fundamentals and Applications*. Springer Science + Business Media LLC, 2007.

[MAL10] Changbao Ma, Ryan Aguinaldo, and Zhaowei Liu. Advances in the hyperlens. *Chinese Science Bulletin*, 55(24):2618–2624, 2010.

[Mar13] Luis Martinez. Single slit interference pattern, Airy disk and resolution. quantumredpill.files.wordpress.com, 2013. Accessed: 2016-08-08.

[MBG+12] E. Mudry, K. Belkebir, J. Girard, J. Savatier, E. Le Moal, C. Nicoletti, M. Allain, and A. Sentenac. Structured illumination microscopy using unknown speckle patterns. *Nature Photonics*, 6(5):312–315, 2012.

[ML10] Changbao Ma and Zhaowei Liu. Focusing light into deep subwavelength using metamaterial immersion lenses. *Optics Express*, 18(5):4838–4844, 2010.

[Mos85] Martin Moskovits. Surface-enhanced spectroscopy. *Reviews of Modern Physics*, 57(3):783–826, 1985.

[MTH12] Keigo Mizusawa, Yousuke Takaoka, and Itaru Hamachi. Specific cell surface protein imaging by extended self-assembling fluorescent turn-on nanoprobes. *Journal of the American Chemical Society*, 134(32):13386–13395, 2012.

[MZC+11] Qingqing Meng, Xiaoping Zhang, Lin Cheng, Pengfei Cao, Yuee Li, Haining Zhang, and Guanghui Wang. Deep subwavelength focusing of light by a trumpet hyperlens. *Journal of Optics*, 13(7):075102, 2011.

[NJW97] M. A. A. Neil, R. Juškaitis, and T. Wilson. Method of obtaining optical sectioning by using structured light in a conventional microscope. *Optics Letters*, 22(24):1905–1907, 1997.

[NLL82] Claes Nylander, Bo Liedberg, and Tommy Lind. Gas detection by means of surface plasmon resonance. *Sensors and Actuators*, 3:79–88, 1982.

[Nov06] Lukas Novotny. *Principles of Nano-Optics*. Cambridge University Press, 2006.

[OSL+13] Keisuke Onishi, Beth Shafer, Charles Lo, Fadel Tissir, Andre M. Goffinet, and Yimin Zou. Antagonistic functions of dishevelleds regulate frizzled3 endocytosis via filopodia tips in wnt-mediated growth cone guidance. *The Journal of Neuroscience*, 33(49):19071–19085, 2013.

[OWZ64] Gerald Oster, Mark Wasserman, and Craig Zwerling. Theoretical interpretation of Moiré patterns. *Journal of the Optical Society of America*, 54(2):169–175, 1964.

[Pal98] Edward D. Palik. *Handbook of Optical Constants of Solids*. Academic Press, 1998.

[PDL84] D. W. Pohl, W. Denk, and M. Lanz. Optical stethoscopy: image recording with resolution λ/20. *Applied Physics Letters*, 44(7):651–653, 1984.

[Pen00] John B. Pendry. Negative refraction makes a perfect lens. *Physical Review Letters*, 85(18):3966–3969, 2000.

[Pen03] John B. Pendry. Perfect cylindrical lenses. *Optics Express*, 11(7):755–760, 2003.

[PWL14] Joseph L. Ponsetto, Feifei Wei, and Zhaowei Liu. Localized plasmon assisted structured illumination microscopy for wide-field high-speed dispersion-independent super resolution imaging. *Nanoscale*, 6:5807–5812, 2014.

[Rae88] Heinz Raether. *Surface Plasmons on Smooth and Rough Surfaces and on Gratings*. Berlin Heidelberg, 1988.

[RBZ06] Michael J. Rust, Mark Bates, and Xiaowei Zhuang. Sub-diffraction-limit imaging by stochastic optical reconstruction microscopy (STORM). *Nature Methods*, 3(10):793–796, 2006.

[RYX+10] Junsuk Rho, Ziliang Ye, Yi Xiong, Xiaobo Yin, Zhaowei Liu, Hyeunseok Choi, Guy Bartal, and Xiang Zhang. Spherical hyperlens for two-dimensional sub-diffractional imaging at visible frequencies. *Nature Communications*, 1(9):143–147, 2010.

[SCB06] Anne Sentenac, Patrick C. Chaumet, and Kamal Belkebir. Beyond the Rayleigh criterion: grating assisted far-field optical diffraction tomography. *Physical Review Letters*, 97(24):243901, 2006.

[SCH+08] Lothar Schermelleh, Peter M. Carlton, Sebastian Haase, Lin Shao, Lukman Winoto, Peter Kner, Brian Burke, M. Cristina Cardoso, David A. Agard, Mats G. L. Gustafsson, Heinrich Leonhardt, and John W. Sedat. Subdiffraction multicolor imaging of the nuclear periphery with 3D structured illumination microscopy. *Science*, 320(5881):1332–1336, 2008.

[SE06] Alessandro Salandrino and Nader Engheta. Far-field subdiffraction optical microscopy using metamaterial crystals: theory and simulations. *Physical Review B*, 74(7):075103, 2006.

[SEG15] Manish Saxena, Gangadhar Eluru, and Sai Siva Gorthi. Structured illumination microscopy. *Advances in Optics and Photonics*, 7(2):241–275, 2015.

[SGAS00] Jan Schmoranzer, Mark Goulian, Dan Axelrod, and Sanford M. Simon. Imaging constitutive exocytosis with total internal reflection fluorescence microscopy. *The Journal of Cell Biology*, 149(1):23–32, 2000.

[Sha06] Kailash K. Sharma. *Optics: Principles and Applications*. Academic Press Burlington, 2006.

[Siy16] Siyavula. Diffraction through a single slit. siyavula.com, 2016. Accessed: 2016-08-08.

[Uni13] Aalto University. Localized plasmon resonance. physics.aalto.fi/wp-content, 2013. Accessed: 2014-06-01.

[Ves68] Viktor G. Veselago. The electrodynamics of substances with simultaneously negative values of ε and μ. *Soviet Physics Uspekhi*, 10(4):509–514, 1968.

[WE79] W. H. Weber and C. F. Eagen. Energy transfer from an excited dye molecule to the surface plasmons of an adjacent metal. *Optics Letters*, 4(8):236–238, 1979.

[WHMH07] Katrin I. Willig, Benjamin Harke, Rebecca Medda, and Stefan W. Hell. STED microscopy with continuous wave beams. *Nature Methods*, 4(11):915–918, 2007.

[WL10] Feifei Wei and Zhaowei Liu. Plasmonic structured illumination microscopy. *Nano Letters*, 10(7):2531–2536, 2010.

[WLS+14] Feifei Wei, Dylan Lu, Hao Shen, Weiwei Wan, Joseph L. Ponsetto, Eric Huang, and Zhaowei Liu. Wide field super-resolution surface imaging through plasmonic structured illumination microscopy. *Nano Letters*, 14(8):4634–4639, 2014.

[Won01] Alfred Wong. *Resolution Enhancement Techniques in Optical Lithography*. SPIE Press Bellingham, 2001.

[WPLon] Weiwei Wan†, Joseph L. Ponsetto†, and Zhaowei Liu. Numerical study of hyperlenses for three-dimensional imaging and lithography. *Optics Express*, 23(14):18501–18510, 2015 [†Equal contribution].

[WVD07] Katherine A. Willets and Richard P. Van Duyne. Localized surface plasmon resonance spectroscopy and sensing. *Annual Review of Physical Chemistry*, 58(1):267–297, 2007.

[XLSZ07] Yi Xiong, Zhaowei Liu, Cheng Sun, and Xiang Zhang. Two-dimensional imaging by far-field superlens at visible wavelengths. *Nano Letters*, 7(11):3360–3365, 2007.

[XLZ09] Yi Xiong, Zhaowei Liu, and Xiang Zhang. A simple design of flat hyperlens for lithography and imaging with half-pitch resolution down to 20 nm. *Applied Physics Letters*, 94(20):203108, 2009.

[ZQS+12] A. Ping Zhang, Xin Qu, Pranav Soman, Kolin C. Hribar, Jin W. Lee, Shaochen Chen, and Sailing He. Rapid fabrication of complex 3D extracellular microenvironments by dynamic optical projection stereolithography. *Advanced Materials*, 24(31):4266–4270, 2012.